



Variation of the Asian summer monsoon since the last glacial-interglacial recorded in a stalagmite from southwest China

Yao Wu ^{a, b, c}, Ting-Yong Li ^{a, b, c, *}, Tsai-Luen Yu ^{d, e}, Chuan-Chou Shen ^{d, e, f}, Chao-Jun Chen ^{a, b, c}, Jian Zhang ^{a, b, c}, Jun-Yun Li ^{a, b, c}, Tao Wang ^{a, b, c}, Ran Huang ^{a, b, c}, Si-Ya Xiao ^{a, b, c}

^a College of Tourism and Geography, Yunnan Normal University, Kunming 650050, China

^b State Cultivation Base of Eco-agriculture for Southwest Mountainous Land, Southwest University, Chongqing, 400715, China

^c Chongqing Key Laboratory of Karst Environment, School of Geographical Sciences, Southwest University, Chongqing 400715, China

^d High-Precision Mass Spectrometry and Environment Change Laboratory (HISPEC), Department of Geosciences, National Taiwan University, Taipei 10617, Taiwan

^e Research Center for Future Earth, National Taiwan University, Taipei 10617, Taiwan

^f Global Change Research Center, National Taiwan University, Taipei 10617, Taiwan



ARTICLE INFO

Article history:

Received 30 October 2019

Received in revised form

1 March 2020

Accepted 2 March 2020

Available online xxx

Keywords:

$\delta^{18}\text{O}$ and $\delta^{13}\text{C}$

Stalagmite

Southwest China

Last glacial-interglacial period

ASM

North-South Hemispheres

Local hydrological conditions

ABSTRACT

A number of studies proposed a close link between the climate changes in the Asian summer monsoon (ASM), the Southern Hemisphere (SH), and high latitudes of the Northern Hemisphere (NH). But the mechanisms is still an open question. Although speleothems $\delta^{18}\text{O}$ records have displayed excellent values in the reconstruction of paleoclimate change at centennial - millennial to orbital timescales, the significance of speleothems $\delta^{18}\text{O}$ and $\delta^{13}\text{C}$ is still debatable. Here, a high-precise ^{230}Th dated stalagmite from southwestern China was used to reconstruct the changes of ASM and regional hydrological conditions since the last interglacial (3.6–118.1 ka BP) by the coupled $\delta^{18}\text{O}$ and $\delta^{13}\text{C}$. We found: (1) The EASM and ISM are synchronous changing on the orbital timescale, responding to the change of North Hemisphere summer insolation (NHSI) and high latitude climate change. There is a teleconnection between Antarctic temperature change and ASM through the Mascarene High and the Somali Jet. (2) During MIS 5d, the stalagmite $\delta^{18}\text{O}$ in Yangzi Cave is nearly 1.5‰ higher than that in MIS 2, the maximum of last glacial. This should be attributed to the different isotopic compositions in moisture source of ISM and EASM, and the dynamic changes of monsoon circulations. (3) From MIS 3 to MIS 2, the ASM showed a “stepped” pattern in weakening, consistent with the decreasing NHSI and increasing global ice volume. (4) The changes in stalagmite $\delta^{13}\text{C}$ indicated the changes of local hydrological conditions and closely correlated with climate changes revealed by stalagmite $\delta^{18}\text{O}$. The effective humidity, which determined by temperature, evaporation, and precipitation, dominated the regional hydrological conditions. The change of effective humidity recorded in stalagmite $\delta^{13}\text{C}$ by influencing surface biomass and soil CO₂-production.

© 2020 Elsevier Ltd. All rights reserved.

1. Introduction

The glacial-interglacial cycle is the main feature of Quaternary climate change, and a series of rapid climatic abrupt events, such as Heinrich events (H events) and Dansgaard-Oeschger events (D/O), are the crucial climatic features of the last glacial interval (Heinrich, 1988; Bond et al., 1993; Dansgaard et al., 1993). These climatic

abrupt events, through the Atlantic meridional overturning circulation (AMOC) and the Northern Hemisphere (NH) mid-latitude westerly winds, affect Asian monsoon changes, as has been widely recorded by stalagmites in the Asian monsoon region (Wang et al., 2001; Yuan et al., 2004; Cai et al., 2006; Zhang et al., 2017).

On the orbital scale, the Asian summer monsoon (ASM) can directly respond to changes in high latitudes Northern Hemisphere summer insolation (NHSI) (21 July, 65°N) and is regulated by the 23 kyr precessional cycles (Wang et al., 2001; Yuan et al., 2004; Cai et al., 2015; Chen et al., 2016; Cheng et al., 2016). Some studies on paleoclimatic records such as ice cores and loess believe that the

* Corresponding author. College of Tourism and Geography, Yunnan Normal University, Kunming 650050, China.

E-mail address: cdtly@swu.edu.cn (T.-Y. Li).

changes in the Antarctic temperature and low-latitudes solar insolation have a positive effect on global climate change (Jouzel et al., 2007; Beck et al., 2018; Nair et al., 2019). The low-latitude tropical regions (30°N - 30°S) receive much more solar insolation than north of 65°N (Beck et al., 2018). In the low latitudes tropical Pacific, especially the Indian Ocean-Pacific warm pool, as vast moisture and heat-exchange source, profoundly impact on ASM (Sirocko, 2003; Qu et al., 2005; Wang et al., 2017). Simulations also show that the convection intensity in the Indian Ocean-Pacific warm pool and low-latitude atmospheric circulation are the main factors controlling the $\delta^{18}\text{O}$ variation of precipitation in ASM (Yang et al., 2016; Cai et al., 2018; Ruan et al., 2019). Therefore, on the orbital scale, comparing high-resolution stalagmite records with driving factors from low latitudes, especially solar insolation, will be more helpful to understand the development and evolution of ASM.

In addition, the phase relationship and coupling mechanism of climate change in the Northern and Southern hemispheres is one of the critical issues in understanding the dynamic changes of the Earth's climate system (EPICA Community Members, 2006). The Southern Hemisphere (SH) abrupt climate change signal can be transmitted from the SH to the Asian monsoon region through atmospheric circulation and ocean-air teleconnection between the Hemispheres (Cai et al., 2006; Chen et al., 2016; Zhang et al., 2016, 2017). Recent researches have shown that Mascarene High and Indian summer monsoon (ISM) plays a leading role in spreading signals of climate change in the SH to the NH (Zhu, 2012; Ding et al., 2018; Nair et al., 2019). However, during the last glacial period, the lack of iceberg-rafterd debris (IRD) records in Southern Ocean, nor high-resolution paleoclimatic records of ice core in low latitudes limited the accurate comparison of climate changes between hemispheres and the Asian monsoon region. This deficiency of present research also hinders the understanding of the phase relationship between the climate changes in East Asian and Antarctic, and the forcing mechanisms of climate change during the last glacial period (Weber et al., 2014; Zhang et al., 2016). Therefore, paleoclimatic records from low latitudes are critical to understanding the interaction of climate between hemispheres and the forcing of the ASM.

There is still debate about the interpretation of stalagmite $\delta^{18}\text{O}$ ($\delta^{18}\text{O}$). Because of the mixed effect of seasonal atmospheric precipitation during the migration in vadose zone above caves, the seasonality of isotopic composition in precipitation is smoothed and the annual weighted average value of local atmospheric precipitation may be represented by the $\delta^{18}\text{O}$ of dripping water in caves (Yonge et al., 1985; Li et al., 2008, 2011). In the ASM region, modern atmospheric observation and simulations have proved that changes in precipitation $\delta^{18}\text{O}$ are mainly affected by large-scale atmospheric dynamics processes, while the influence of regional rainfall amount is limited (Tan, 2014; Li, 2018). The lower $\delta^{18}\text{O}$ may be the result of the upstream rainout and enhancement of the summer monsoon circulation or monsoon intensity, but the rainfall amount in East Asian summer monsoon (EASM) regions does not necessarily increase anywhere (Midhun and Ramesh, 2016; Yang et al., 2016; Cai et al., 2018; Ruan et al., 2019). Long-term cave monitoring in EASM regions has also proved that the variation of cave drip water $\delta^{18}\text{O}$ on seasonal-interannual time scale can reflect the variation of precipitation $\delta^{18}\text{O}$ caused by large-scale atmospheric circulation (such as ENSO) (Chen and Li, 2018; Zhang and Li, 2019). Although other interpretations exist, one interpretation is that the stronger NHI, the stronger ASM intensity, the higher ratio of precipitation between summer and winter, and the lower $\delta^{18}\text{O}$ (Wang et al., 2001, 2005; Cheng et al., 2016). This inference has been widely accepted and broadly consistent with both theoretical and empirical studies on orbital to millennial timescales (Chen

et al., 2016; Zhang et al., 2016, 2017, 2019).

In contrast to $\delta^{18}\text{O}$, complex factors of climatic and cave processes influence stalagmite $\delta^{13}\text{C}$ ($\delta^{13}\text{C}$) and have limited the application of $\delta^{13}\text{C}$ in the reconstruction of paleoclimate and paleoenvironment. The changes of $\delta^{13}\text{C}$ were usually interpreted as vegetation types, regional temperature and humidity variations on millennium-orbital time scale (Bar-Matthews et al., 1997; Dorale et al., 1998; Fleitmann et al., 2009; Zhang et al., 2019). But, in low latitudes (e.g., South monsoon China), although the temperature and vegetation coverage declined during the Last Glacial Maximum (LGM), the vegetation types did not change fundamentally (Wang et al., 2012; Xue et al., 2015; Li et al., 2013; Li et al., 2018). However, the change of regional hydrological conditions controlled by temperature and precipitation have a profound effect on surface vegetation, soil microbial activity, and soil CO_2 yield, which has been supported by stalagmite researches and field monitoring (Cosford et al., 2009; Kuo et al., 2011; Liu et al., 2016; Li et al., 2018). Recent studies also suggested that changes in local hydrological conditions can be reflected by the $\delta^{13}\text{C}$ in cave drip water and stalagmite. That is lower $\delta^{13}\text{C}$ values in drip water and stalagmite when precipitation and soil effective humidity increased; conversely, $\delta^{13}\text{C}$ will become higher (Liu et al., 2016; Li and Li, 2018; Li et al., 2018).

Although $\delta^{13}\text{C}$ has been used in the reconstruction of paleoclimate and paleoenvironment in a few case studies (Bar-Matthews et al., 1997; Genty et al., 2003; Kong et al., 2005; Cosford et al., 2009; Fleitmann et al., 2009; Liu et al., 2016; Zhang et al., 2019), under the influence of local environmental conditions, the original signal of $\delta^{13}\text{C}$ in surface are often distorted by the transport processes in epikarst zone and the environmental changes in cave (e.g. cave ventilation, air pCO_2 , drip rate, and humidity) (Hendy, 1971; Mickler et al., 2004; Fairchild et al., 2006; Spötl et al., 2005; Dreybrodt and Scholz, 2011; Li et al., 2012, 2018), making it difficult to accurately interpret the original signals of $\delta^{13}\text{C}$. Although the original $\delta^{13}\text{C}$ signal of soil CO_2 may be disturbed by these inorganic factors, these factors are mainly driven by the changes of local climate and environment (McDermott, 2004; Fairchild et al., 2006; Liu et al., 2016; Li et al., 2018), combining $\delta^{13}\text{C}$ with $\delta^{18}\text{O}$ to explore the influencing factors, changing process and indicated climatic environment significance of $\delta^{13}\text{C}$ in different climate backgrounds is still essential for promoting paleoclimate and regional environmental reconstruction.

Using $\delta^{18}\text{O}$ and $\delta^{13}\text{C}$ records of stalagmite YZ1 in Yangzi cave, Southwest China, we reconstructed the changes of the ASM and regional hydrological environment at the orbital-millennial scale during the last ice age. By comparing with other paleoclimatic records, it is found that the EASM and ISM are synchronous on the orbital scale of the last glacial, and the change of ASM intensity during the last glacial-interglacial period are affected by NH low latitude summer insolation and Antarctic temperature change. YZ1 $\delta^{18}\text{O}$ and $\delta^{13}\text{C}$ have coupled characteristics, and $\delta^{13}\text{C}$ can reflect the changes of regional hydrology and ecological environment under the control of ASM.

2. Material and methods

2.1. Yangzi cave and local geography

Yangzi cave ($29^{\circ}47'\text{N}$, $107^{\circ}47'\text{E}$, 400 m above sea level, and ~500 long) is located in the lower reaches of Longhe River, a tributary of the Yangtze River in Fengdu County, Chongqing City, Southwest China (Fig. 1), developed in lower Triassic limestone with a length of about 500 m (Zhu et al., 2004). The region belongs to the subtropical humid monsoon climate, which is affected by East Asian

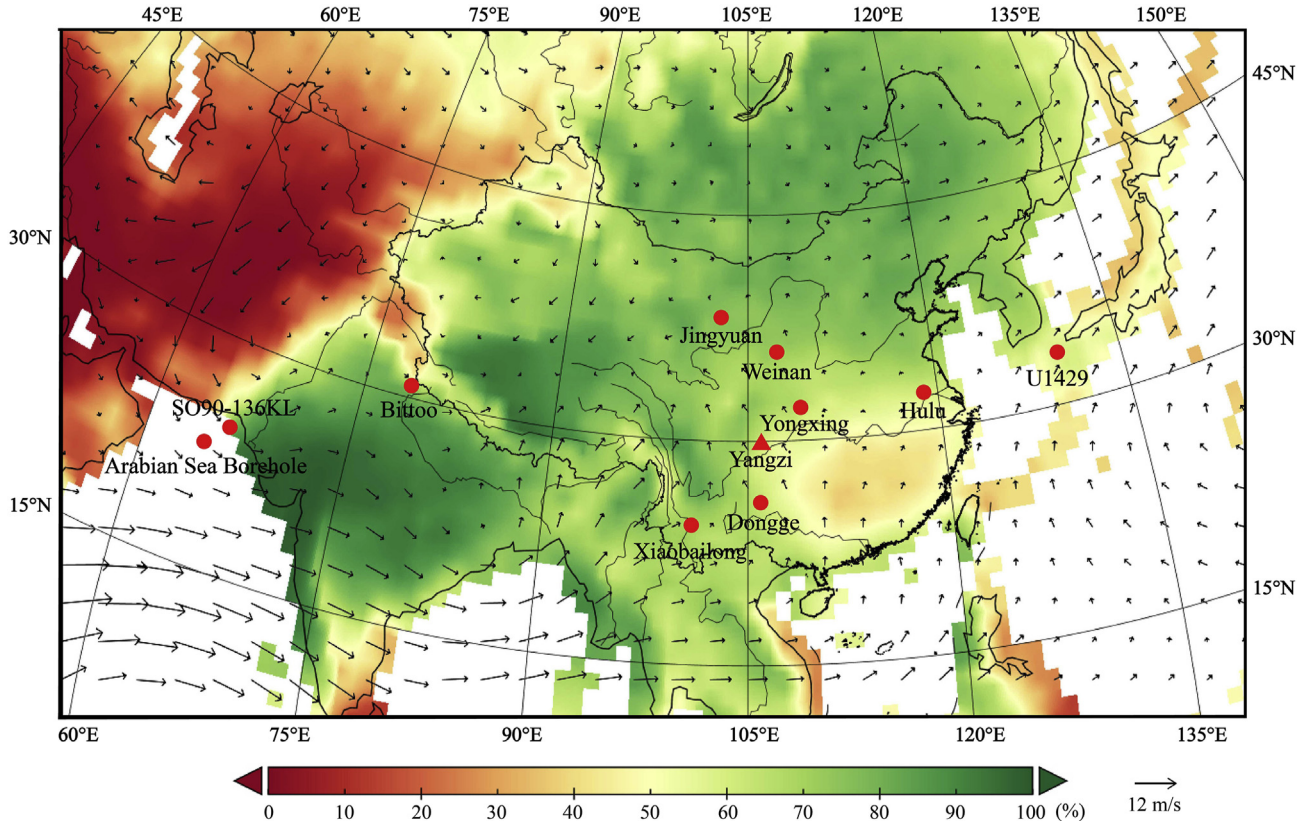


Fig. 1. Long-term (1981–2018) percentage of summer precipitation (June–September) based on the $1.0^\circ \times 1.0^\circ$ gridded gauge-analysis data from the GPCC (Global Precipitation Climatology Center) precipitation V2018 combined. The arrows indicate the summer (June–September) 850-hPa wind field. Wind data are derived from the NCEP/NCAR reanalysis datasets, with averages calculated over the period of 1981–2018. The Red triangle represent the Yangzi Cave (This study), red dots represent the Dongge Cave (Yuan et al., 2004), Hulu Cave (Wang et al., 2001), Yongxing Cave (Chen et al., 2016), Xiaobailong Cave (Cai et al., 2015), Jingyuan Loess (Sun et al., 2010), Bittoo Cave (Kathayat et al., 2016), Arabian Sea sediment cores SO130-289 KL (Deplazes et al., 2013) and S90-136 KL (Schulz et al., 1998), and International Ocean Discovery Program sediment cores U1429 (Clemens et al., 2018), respectively. The map was created using Panoply (Version 4.10.12, available at <https://www.giss.nasa.gov/tools/pa>). (For interpretation of the references to color in this figure legend, the reader is referred to the Web version of this article.)

and Indian monsoons (Fig. 1). It has four distinct seasons throughout the year. It is cold and dry in winter and hot and rainy in summer (Zhu et al., 2004). Instrumental climate data from the nearest meteorological station, Fengdu station (18 km northwest of Yangzi Cave), indicate the mean annual temperature and precipitation are $18.3\text{ }^\circ\text{C}$ and 1018.6 mm respectively, and summer precipitation (June–October) accounts for 70% of the whole year (1980–2010 averages, according to Chinese Meteorological Administration data at <http://www.cma.gov.cn/>). Mean cave temperature is approximately constant at $16\text{ }^\circ\text{C}$, and the humidity is close to 100% (Li, 2007; Xu et al., 2013). Modern densely forested vegetation above Yangzi Cave consists primarily of perennial subtropical evergreen broad-leaved forest (C3-type vegetation) and shrubs, including *Pinus massoniana*, *Cyclobalanopsis glauca* and *Pistacia chinensis*, etc (Pu et al., 2009).

2.2. Sample and methods

YZ1 stalagmite was collected about 200 m away from the entrance of the cave. The stalagmite is 69 cm in length, approximately 10 cm and 6.5 cm in diameter at the bottom and top, respectively. After cutting along the growth axis of the stalagmite, it can be seen that YZ1 stalagmite is composed of pure and dense calcite, and its color is mainly white (Fig. 2A).

On the polishing surface of YZ1 stalagmite, 50–100 mg powder for U–Th dating was drilled with a 1 mm diameter dental drill parallel to the growth layer. A total of 58 U–Th dating samples were

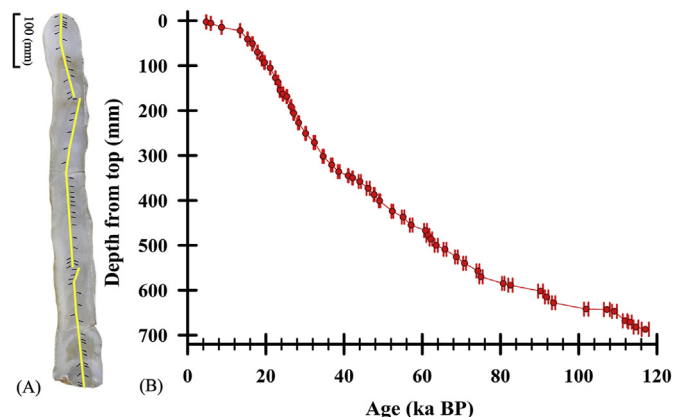


Fig. 2. Age model of stalagmite YZ1. (A) A polished picture of YZ1 stalagmite. The yellow band indicates the sampling trajectory of 1300 samples of $\delta^{18}\text{O}$ and $\delta^{13}\text{C}$, and the black bars indicate positions of the 58 U–Th dates used to construct the chronology. (B) The age model of the YZ1 stalagmite. The red dots are the depth and age of the U–Th dating sample, and the error bars indicate the dating error ($\pm 2\sigma$). The chronological model of the YZ1 stalagmite record was established by linear interpolation. (For interpretation of the references to color in this figure legend, the reader is referred to the Web version of this article.)

obtained from top to bottom (Fig. 2A). Dating was performed at the High-Precision Mass Spectrometry and Environment Change Laboratory (HISPEC), Department of Geosciences, National Taiwan

University, using multi-collector inductively coupled plasma mass spectrometry (MC-ICP-MS). The decay constants of ^{230}Th , ^{234}U , and ^{238}U used are $9.1705 \times 10^{-6} \text{ yr}^{-1}$, $2.82206 \times 10^{-6} \text{ yr}^{-1}$ (Cheng et al., 2013), and $1.55125 \times 10^{-10} \text{ yr}^{-1}$ (Jaffey et al., 1971), respectively. Age correction for the initial ^{230}Th was performed using the average crustal $^{230}\text{Th}/^{232}\text{Th}$ ratio of $4.4 \pm 2.2 \times 10^{-6}$ (Taylor and McLennan, 1995).

On the polished section of YZ1 stalagmite, 1300 stable carbon and oxygen isotope samples were drilled along the growth axis with a 0.5 mm diameter dental drill (Fig. 2A). Analyses were performed on a Delta V Plus isotope ratio mass spectrometer equipped with a Kiel IV Carbonate Device at the Geochemistry and Isotope Laboratory of Southwest University, China. One standard sample was inserted per 7 samples (SWU-1), and results are given with respect to the Vienna Pee Dee Belemnite (V-PDB), with a one-sigma external error is $< 0.1\text{\textperthousand}$ for $\delta^{18}\text{O}$ and $< 0.06\text{\textperthousand}$ for $\delta^{13}\text{C}$.

3. Results

3.1. ^{230}Th dating and age model

The ^{238}U concentration of YZ1 stalagmite ranged from 53 to 1794 ppb, $^{230}\text{Th}/^{232}\text{Th}$ ratio ranged from 271×10^{-6} to $982,000 \times 10^{-6}$, and age error was calculated at 2σ , with an average error of 269 years. (Table 1). There was no apparent hiatus during the growth of YZ1 stalagmite. All dates are in stratigraphic order and U and Th isotopic compositions and ^{230}Th dates are given in Table 1, which provides precise chronological control for YZ1 stalagmite records.

Among the 58 dating results of YZ1 stalagmite, the ages of the top and bottom samples were $4.695 \pm 0.071 \text{ ka BP}$ and $116.83 \pm 0.92 \text{ ka BP}$, respectively. The age model of YZ1 stalagmite was established by linear interpolation (Fig. 2B), the sedimentary period of the whole stalagmite is 3.68–118.17 ka BP, and the average resolution is about 88 years, covering the entire last glacial period. The average growth rate of YZ1 stalagmite is 6.04 mm/ka. During the deposition, the growth axis shifted at the depth of 83 mm (18.83 ka BP), 160 mm (23.73 ka BP), and 475 mm (61.12 ka BP) from top. Deposition rates at different stages are also quite different. The deposition rates are faster at 85–163 mm (19.01–24.37 ka BP) from the top (15.80 mm/ka) and slower at 585–687 mm (80.71–116.8 ka BP) from the top (3.8 mm/ka).

3.2. $\delta^{18}\text{O}$ and $\delta^{13}\text{C}$ stable isotope composition

The variation range of $\delta^{18}\text{O}$ and $\delta^{13}\text{C}$ of YZ1 stalagmite is $-9.7\text{\textperthousand}$ to $-4.7\text{\textperthousand}$ and $-11.6\text{\textperthousand}$ to $-6.5\text{\textperthousand}$, respectively, the average values are $-8.1\text{\textperthousand}$ and $-9.9\text{\textperthousand}$, respectively, with a mean temporal resolution of ~88 years (Table S1). The total $\delta^{18}\text{O}$ and $\delta^{13}\text{C}$ sequence is characterized by the recurrence of a series of fluctuations on the millennium timescale, show clear correlative patterns of change, and the correlation coefficient between them is $r = 0.64$ ($p < 0.01$), with minimum and maximum values occurring at ~34 to 38 ka BP and ~116–118 ka BP, respectively (Fig. 3).

3.3. Test of equilibrium deposition

The “replication principle” by comparing overlapping $\delta^{18}\text{O}$ profiles has been proved is an effective method in assessing the possibility of calcite deposition under isotopic equilibrium conditions (Dorale and Liu, 2009). Both Yangzi Cave and Yangkou Cave are located in Chongqing and approximately 100 km away with each other. The $\delta^{18}\text{O}$ patterns of the YZ1 and JFYK7 records agreed well with each other during the overlapping period of 40–80 ka BP (Han et al., 2016; Zhang et al., 2017) (Fig. S1), and are consistent

with the other $\delta^{18}\text{O}$ records from central and eastern China (Fig. 4). These repeatability indicated that there was negligible kinetic isotope fractionation during the deposition of stalagmite YZ1 and the change of YZ1 $\delta^{18}\text{O}$ mainly reflected climate change.

4. Discussion

4.1. YZ1 $\delta^{18}\text{O}$ and $\delta^{13}\text{C}$ time series

4.1.1. The $\delta^{18}\text{O}$ records

The whole $\delta^{18}\text{O}$ record shows fluctuations of 1–1.5‰ near the average (except for MIS 5d), the lowest $\delta^{18}\text{O}$ values of $-11.6\text{\textperthousand}$ are observed during the MIS 3 (34.4 ka BP), while the highest of $-6.5\text{\textperthousand}$ is during the MIS 5d (112.2 ka BP). The five distinct negative periods in $\delta^{18}\text{O}$ record and their average values are MIS1 ($-8.3\text{\textperthousand}$), early ($-8.7\text{\textperthousand}$) and late ($-8.8\text{\textperthousand}$) of MIS3, MIS 5a ($-8.6\text{\textperthousand}$), and MIS 5c ($-8.7\text{\textperthousand}$), respectively, corresponding to the stronger NHSI (Fig. 3A). The $\delta^{18}\text{O}$ values were significantly positive in MIS 2 ($-7.4\text{\textperthousand}$), MIS 4 ($-7.7\text{\textperthousand}$), MIS 5b ($-7.4\text{\textperthousand}$), and MIS 5d ($-6.4\text{\textperthousand}$). Although the $\delta^{18}\text{O}$ was relatively positive ($-8.19\text{\textperthousand}$) in the middle stage of MIS3 (37.7–48.0 ka BP), but overall was still lighter than the average ($-8.0\text{\textperthousand}$). The transition from the late glacial to Holocene was marked by abrupt changes in $\delta^{18}\text{O}$ during the onset of the H1 and the B/A (Fig. 3A). The evolution of the whole $\delta^{18}\text{O}$ record closely follows NHSI curve and agreed with recodes previously published from other Chinese caves.

The six abrupt positive excursion of $\delta^{18}\text{O}$ (~1.5‰ amplitude) at 15.1, 24.1, 30.2, 39.4, 47.6, and 60.3 ka BP, corresponded to H events 1–6 (H1–H6), respectively (Fig. 3A), and similar to other records in ASM regions (Fig. 4). In the whole YZ1 $\delta^{18}\text{O}$ records, obviously negative shifts with an amplitude of 0.6‰–1‰ can be identified on the millennial scale, corresponding to D/O events 1–25 respectively (Fig. 3A). However, D/O 23 and D/O 25 were not obvious, which may be related to the lack of more age-controlling points and the lower temporal resolution of $\delta^{18}\text{O}$ (167a, twice the average resolution) in this period (90.0–118.1 ka BP).

4.1.2. The $\delta^{13}\text{C}$ records

Compared with $\delta^{18}\text{O}$, the $\delta^{13}\text{C}$ records of YZ1 also characterized persistent millennial-scale oscillations between $-11.6\text{\textperthousand}$ and $-6.5\text{\textperthousand}$ (Fig. 3B). The $\delta^{13}\text{C}$ maintained lower average values during MIS 1, MIS 3, MIS 5a, and MIS 5c, which were $-10.0\text{\textperthousand}$, $10.3\text{\textperthousand}$, $10.7\text{\textperthousand}$, $10.4\text{\textperthousand}$, respectively. On the contrary, the average values of $\delta^{13}\text{C}$ during MIS 2, MIS 4, MIS 5b, and MIS 5d were $-8.7\text{\textperthousand}$, $-9.9\text{\textperthousand}$, $-9.7\text{\textperthousand}$, $-8.9\text{\textperthousand}$, respectively. When H events occurred, the $\delta^{13}\text{C}$ values abruptly increased by an average of ~1.8‰, with the amplitude of 1.0–3.5‰. In general, the change of $\delta^{13}\text{C}$ was similar to the of $\delta^{18}\text{O}$.

However, in some periods, the millennial $\delta^{13}\text{C}$ oscillations presented larger amplitude than the $\delta^{18}\text{O}$, e.g., at 30.2 (H3), 24.1 (H2), and 21.2 ka BP. During these periods, the $\delta^{13}\text{C}$ values were suddenly increased 3.3‰, 3.0‰, and 3.2‰, respectively (Fig. 3B). While the amplitude of $\delta^{18}\text{O}$ variations was only ~1.5‰ (Fig. 3A).

The $\delta^{13}\text{C}$ values remained relative stable during the early and middle MIS 3, overall stayed above the average (Fig. 3B). The two positive excursions of $\delta^{13}\text{C}$ values in this period were corresponding to H4 and H5 (Fig. 3B). During the transition from MIS 3 to MIS 2, other two dramatic positive excursions of $\delta^{13}\text{C}$ were well consistant with H3 and H2 (Fig. 3B). In the last glacial, the highest $\delta^{13}\text{C}$ value of YZ1 was $-7.1\text{\textperthousand}$, occurred at 24.7 ka BP in the H 2 event. After that time, the $\delta^{13}\text{C}$ values were steadily tending to more negative in frequently fluctuations.

Table 1

Uranium-series dating results for stalagmite YZ1, dated in the high-precision mass spectrometry and environment change laboratory (HISPEC) of National Taiwan University.

Sample ID	Depth (mm)	^{238}U	^{232}Th	$\delta^{234}\text{U}$	$[^{230}\text{Th}/^{238}\text{U}]$	$[^{230}\text{Th}/^{232}\text{Th}]$	Age (ka. BP)	Age (ka. BP)	$\delta^{234}\text{U}_{\text{initial}}$
		ppb	ppt	measured ^a	activity ^c	ppm ^d	uncorrected	corrected ^e	corrected ^b
YZ1-1	3	153.6±0.3	2447±23.8	5039.6±12.0	0.2619±0.0033	271±4	4.764±0.062	4.695±0.071	5107.6±12.2
YZ1-2	6	177.3±0.4	302±8.5	5107.5±15.1	0.3270±0.0015	3169±90	5.917±0.032	5.910±0.032	5194.2±15.4
YZ1-3	15	103.3±0.2	199±4.1	5114.2±13.7	0.4749±0.0017	4070±85	8.666±0.038	8.666±0.038	5241.9±14.0
YZ1-4	17	88.3±0.1	153±4.1	5126.7±5.1	0.5746±0.0018	5465±146	10.600±0.036	10.523±0.036	5282.2±5.3
YZ1-5	19	90.4±0.1	107±4.6	5129.3±5.5	0.6434±0.0019	8985±384	11.917±0.038	11.843±0.038	5304.6±5.7
YZ1-6	22	109.2±0.2	68±3.4	5172.2±15.2	0.7274±0.0019	19232±972	13.430±0.051	13.427±0.051	5372.8±15.8
YZ1-7	41	156.1±0.4	173±3.1	5170.5±25.2	0.8236±0.0025	12295±225	15.315±0.083	15.311±0.083	5399.6±26.4
YZ1-8	51	239.6±0.7	610±5.6	5162.3±33.0	0.8860±0.0032	5743±54	16.570±0.114	16.560±0.114	5410.1±34.7
YZ1-9	70	208.2±0.4	66±4.8	5158.4±21.1	0.9498±0.0029	49407±3604	17.856±0.088	17.855±0.088	5425.8±22.3
YZ1-10	85	210.4±0.5	137±5.7	5165.6±28.9	1.0088±0.0033	25633±1063	19.021±0.117	19.018±0.117	5451.2±30.6
YZ1-11	93	230.3±0.6	149±4.7	5161.3±25.2	1.0392±0.0033	26486±841	19.651±0.110	19.648±0.110	5456.4±26.7
YZ1-12	105	203.0±0.2	1263±6.9	5138.7±8.7	1.1068±0.0028	2937±17	21.113±0.066	21.088±0.067	5454.6±9.3
YZ1-13	127	294.0±0.3	26±5.5	5120.6±5.8	1.1683±0.0025	214806±44837	22.455±0.057	22.455±0.057	5456.4±6.2
YZ1-14	137	282.5±0.4	245±4.5	5104.7±12.3	1.1970±0.0027	22823±423	23.119±0.077	23.116±0.077	5449.6±13.2
YZ1-15	155	226.6±0.6	23±4.9	5097.8±25.6	1.2202±0.0039	198831±42168	23.637±0.136	23.637±0.136	5450.2±27.5
YZ1-16	163	140.7±0.3	142±8.1	5108.4±16.8	1.2574±0.0041	20539±1170	24.376±0.114	24.372±0.114	5472.9±18.1
YZ1-17	169	246.2±0.5	31±3.2	5085.5±19.8	1.2996±0.0034	172268±17846	25.374±0.116	25.374±0.116	5463.8±21.4
YZ1-18	191	275.4±0.5	6±4.5	5059.1±14.9	1.3434±0.0035	982387±703719	26.440±0.105	26.440±0.105	5451.8±16.2
YZ1-19	206	209.8±0.5	7±5.2	5075.8±19.6	1.3795±0.0040	651542±458218	27.140±0.129	27.140±0.129	5480.6±21.3
YZ1-20	227	1794.0±4.6	459±4.2	5050.5±22.8	1.4298±0.0050	92341±864	28.364±0.162	28.363±0.162	5472.1±24.8
YZ1-21	251	186.5±0.4	186±8.2	5004.2±14.1	1.5002±0.0047	24862±1098	30.176±0.132	30.172±0.132	5449.6±15.5
YZ1-22	271	127.6±0.4	71±5.3	4943.0±26.8	1.5829±0.0061	47183±3519	32.408±0.217	32.406±0.217	5417.0±29.6
YZ1-23	302	133.9±0.3	38±3.9	4909.9±19.3	1.6705±0.0056	96498±9776	34.654±0.184	34.652±0.184	5414.9±21.5
YZ1-24	321	104.2±0.3	46±7.9	4894.4±20.2	1.7580±0.0070	66168±11413	36.830±0.222	36.828±0.222	5431.1±22.7
YZ1-25	336	210.3±0.5	33±5.5	4852.5±24.1	1.8196±0.0065	190306±31495	38.622±0.242	38.621±0.242	5411.9±27.1
YZ1-26	345	197.0±0.2	138±4.5	4864.9±6.1	1.9270±0.0032	45570±1489	41.064±0.093	41.064±0.093	5464.5±7.1
YZ1-27	350	182.8±0.2	122±3.6	4857.7±6.3	1.9698±0.0036	48757±1443	42.182±0.104	42.182±0.104	5473.8±7.3
YZ1-28	358	163.5±0.5	144±5.0	4651.1±23.1	1.9669±0.0077	36945±1277	44.025±0.292	44.021±0.292	5266.8±26.5
YZ1-29	373	159.2±0.7	34±5.4	4627.8±32.6	2.0388±0.0102	159819±25776	46.142±0.419	46.141±0.419	5271.8±37.6
YZ1-30	387	191.5±0.2	31±4.0	4639.8±9.9	2.1010±0.0043	212041±27289	47.687±0.154	47.686±0.154	5308.5±11.6
YZ1-31	401	180.5±0.3	15±5.2	4603.6±13.1	2.1384±0.0050	422735±146653	49.073±0.194	49.072±0.194	5287.7±15.3
YZ1-32	424	161.0±0.3	16±4.7	4526.4±15.3	2.2250±0.0061	370244±108633	52.332±0.246	52.331±0.246	5247.0±18.1
YZ1-33	437	209.4±0.5	20±4.3	4501.2±19.7	2.3104±0.0071	401885±86133	55.077±0.317	55.076±0.317	5258.3±23.5
YZ1-34	455	111.2±0.3	252±4.8	4469.3±18.5	2.3679±0.0083	17250±334	57.165±0.344	57.155±0.344	5251.6±22.4
YZ1-35	456	118.3±0.1	260±3.7	4424.5±4.8	2.4144±0.0046	18103±259	58.995±0.154	58.917±0.154	5225.9±6.1
YZ1-36	461	135.8±0.1	115±4.0	4430.9±4.2	2.4298±0.0043	47422±1661	59.370±0.142	59.298±0.142	5239.1±5.4
YZ1-37	463	134.6±0.1	120±3.8	4425.3±4.8	2.4367±0.0043	44907±1400	59.657±0.144	59.584±0.144	5236.7±6.0
YZ1-38	467	162.1±0.4	411±5.6	4413.8±18.7	2.4647±0.0087	16046±223	60.828±0.376	60.817±0.376	5240.2±22.9
YZ1-39	478	183.0±0.5	137±4.7	4424.6±19.5	2.4900±0.0084	54879±1866	61.450±0.379	61.446±0.379	5262.4±23.8
YZ1-40	486	171.0±0.4	56±7.9	4408.1±14.8	2.5067±0.0081	126688±17845	62.202±0.330	62.201±0.330	5253.9±18.3
YZ1-41	500	173.5±0.4	72±6.3	4369.9±19.8	2.5322±0.0093	100404±8721	63.564±0.418	63.562±0.418	5228.4±24.4
YZ1-42	509	117.2±0.2	212±4.7	4328.7±14.8	2.5823±0.0088	23547±521	65.795±0.367	65.788±0.367	5211.6±18.7
YZ1-43	526	134.6±0.3	70±7.3	42874±12.1	2.6515±0.0080	84579±8889	68.732±0.335	68.730±0.335	5204.8±15.5
YZ1-44	540	126.5±0.2	17±3.3	4252.5±14.4	2.6961±0.0077	332207±64485	70.826±0.364	70.825±0.364	5193.0±18.4
YZ1-45	557	123.0±0.2	7±4.8	4141.6±12.9	2.7356±0.0082	782265±527177	74.232±0.381	74.232±0.381	5106.3±16.8
YZ1-46	570	156.4±0.3	26±2.9	41774±16.2	2.7770±0.0087	277096±31027	75.008±0.437	75.007±0.437	5161.7±21.0
YZ1-47	585	79.0±0.1	147±3.8	4083.4±9.9	2.8875±0.0058	25637±664	80.710±0.304	80.710±0.304	5130.6±13.2
YZ1-48	589	53.2±0.1	40±4.7	4019.5±13.8	2.8925±0.0118	63246±7383	82.557±0.549	82.554±0.549	5073.2±19.1
YZ1-49	602	150.3±0.4	184±4.8	3975.7±18.7	3.0599±0.0097	41170±1070	90.241±0.622	90.236±0.622	5127.5±25.7
YZ1-50	615	163.2±0.2	682±4.6	3956.1±10.8	3.0854±0.0076	12193±86	91.799±0.424	91.781±0.424	5124.5±15.3
YZ1-51	628	117.7±0.2	60±3.8	3939.4±11.2	3.1174±0.0073	100949±6465	93.583±0.431	93.581±0.431	5128.7±15.8
YZ1-52	642	74.1±0.1	27±4.8	3793.5±13.8	3.2098±0.0080	143112±25225	101.925±0.571	101.923±0.571	5056.0±20.1
YZ1-53	643	66.8±0.1	1373±5.7	3671.5±8.6	3.2359±0.0141	2601±15	107.209±0.763	107.118±0.764	4965.3±15.8
YZ1-54	647	104.1±0.2	1395±4.7	3668.7±12.9	3.2728±0.0088	4033±16	109.129±0.636	109.069±0.636	4988.8±19.7
YZ1-55	668	152.1±0.3	683±7.7	3594.0±9.2	3.2723±0.0091	12023±137	111.850±0.582	111.829±0.582	4925.3±15.0
YZ1-56	671	150.6±0.2	439±3.5	3538.7±7.5	3.2559±0.0067	18428±148	113.112±0.457	113.099±0.457	4866.8±12.0
YZ1-57	682	167.5±0.3	1984±9.3	3470.9±8.2	3.2344±0.0096	4507±24	114.645±0.616	114.591±0.616	4793.6±14.1
YZ1-58	687	188.7±0.3	7799±25.5	3401.8±7.1	3.2258±0.0154	1289±7	117.023±0.917	116.832±0.921	4727.8±15.7

Analytical errors are 2s of the mean.

$$^a \delta^{234}\text{U} = ([^{234}\text{U}/^{238}\text{U}]_{\text{activity}} - 1) \times 1000.$$

$$^b \delta^{234}\text{U}_{\text{initial corrected}} \text{ was calculated based on } {}^{230}\text{Th age (T)}, \text{ i.e., } \delta^{234}\text{U}_{\text{initial}} = \delta^{234}\text{U}_{\text{measured}} \times e^{\lambda^{234}\text{U} T}, \text{ and T is corrected age.}$$

$$^c [{}^{230}\text{Th}/{}^{238}\text{U}]_{\text{activity}} = 1 - e^{-\lambda^{230}\text{T}} + (\delta^{234}\text{U}_{\text{measured}}/1000)(\lambda^{230}/(\lambda^{230} - \lambda^{234})) (1 - e^{-(\lambda^{230} - \lambda^{234}) T}), \text{ where T is the age. Decay constants are } 9.1705 \times 10^{-6} \text{ yr}^{-1} \text{ for } {}^{230}\text{Th}, 2.82206 \times 10^{-6} \text{ yr}^{-1} \text{ for } {}^{234}\text{U} \text{ (Cheng et al., 2013), and } 1.55125 \times 10^{-10} \text{ yr}^{-1} \text{ for } {}^{238}\text{U} \text{ (Jaffey et al., 1971).}$$

$$^d \text{ The degree of detrital } {}^{230}\text{Th contamination is indicated by the } [{}^{230}\text{Th}/{}^{232}\text{Th}] \text{ atomic ratio instead of the activity ratio.}$$

$$^e \text{ Age corrections for samples were calculated using an estimated atomic } {}^{230}\text{Th}/{}^{232}\text{Th ratio of } 4 \pm 2 \text{ ppm. Those are the values for a material at secular equilibrium, with the crustal } {}^{232}\text{Th}/{}^{238}\text{U value of 3.8. The errors are arbitrarily assumed to be 50%.}$$

4.2. Comparison between YZ1 $\delta^{18}\text{O}$ and other climate records

4.2.1. Similar patterns for the climate change in EASM

A series of abrupt climatic events since the last glacial period,

including the YD, H1–H6 and D/O cycles, have been recorded in the Greenland ice cores (Heinrich, 1988; Dansgaard et al., 1993). The change of ASM was closely related to climate change in the high latitudes of NH on millennium timescale via large scale ocean-

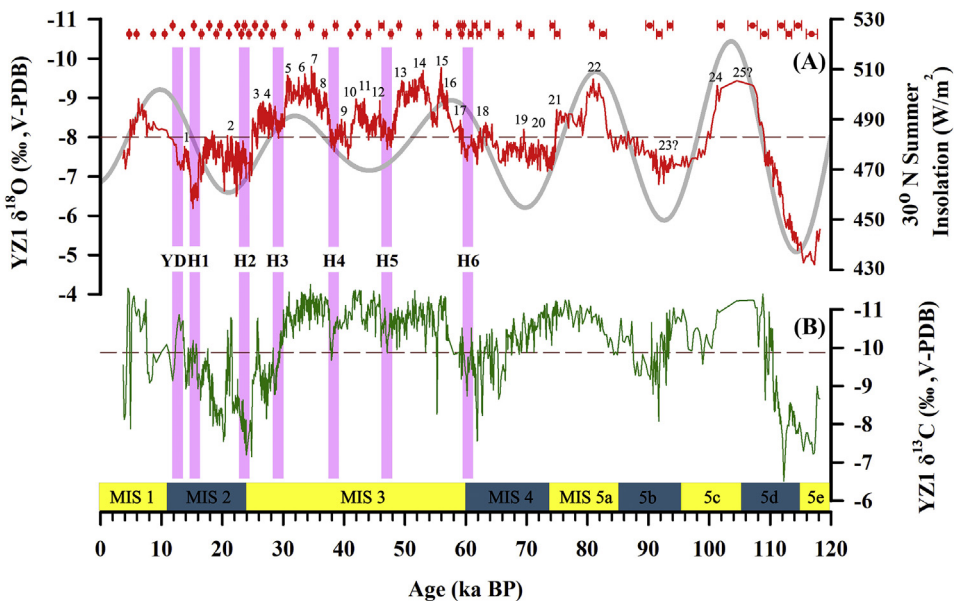


Fig. 3. YZ1 stalagmite $\delta^{18}\text{O}$ (A) and $\delta^{13}\text{C}$ (B) records; red dots are the depth and age of the U-Th dating samples, and the error bars indicate the dating error ($\pm 2\sigma$). The brown dotted lines show the average values of $\delta^{18}\text{O}$ ($-8.0\text{\textperthousand}$) and $\delta^{13}\text{C}$ ($-9.9\text{\textperthousand}$), respectively. The gray curve shows the 30°N summer insolation (Berger and Loutre, 1991). The pink vertical bars indicate YD and H events (Heinrich, 1988); the Arabic numbers indicate the D-O event (Dansgaard et al., 1993). The yellow and cyan bands along X-axis indicate Marine Isotope Stages (MIS) (Lisiecki and Raymo, 2005; NEEM Community Members, 2013). (For interpretation of the references to color in this figure legend, the reader is referred to the Web version of this article.)

atmosphere coupling (Wang et al., 2001; Sun et al., 2010; Chen et al., 2016) (Fig. 4). All those abrupt climatic events mentioned above were demonstrated clearly by the excursions in YZ1 $\delta^{18}\text{O}$ records too (Fig. 3), and consistent with other climatic records in Asian monsoon regions (Wang et al., 2001; Sun et al., 2010; Chen et al., 2016) (Fig. 4). During MIS 4 and MIS 2, responding to the decrease of NHSI, $\delta^{18}\text{O}$ values of stalagmite YZ1 were higher than the average value of $-8.0\text{\textperthousand}$ (Fig. 3A). MIS 2 exhibited the coldest climate and the largest global ice volume during the last glacial period (Lisiecki and Raymo, 2005). A series of abrupt climatic events, such as H and D/O cycles, were clearly recorded in the $\delta^{18}\text{O}$ of stalagmite YZ1 during the period of MIS 2 than that in MIS 4, and consistent with the change of winter monsoon intensity (Fig. 3A; Fig. 4A) (Sun et al., 2010).

4.2.2. The relationship between EASM and ISM

ISM and EASM are essential components of ASM (Tao and Chen, 1987; Ding et al., 2018). Previous researches proved that both the phase relationship between ISM and EASM, and the driving factors, are complicated on different time scales (Hong et al., 2014; Jiang et al., 2014; Cai et al., 2015; Kathayat et al., 2016). In contrast to the stalagmites $\delta^{18}\text{O}$ records from Southwest China influenced by ISM (Zhao et al., 2010; Jiang et al., 2014; Cai et al., 2015), Yangzi cave locates more northeastward, and influenced by both the ISM and EASM (Fig. 1).

There are series of millennial-scale climate events (such as H and YD) in YZ1 and other records from ISM and EASM regions (Fig. 5) (Schulz et al., 1998; Wang et al., 2001; Deplazes et al., 2013; Kathayat et al., 2016). During each H events, both EASM and ISM weakened significantly (Figs. 4 and 5), accompanied by a southward shift of the Intertropical convergence Zone (ITCZ) (Fig. 5F). For example, after the termination of H1 (~14–15 ka BP), the stalagmite $\delta^{18}\text{O}$ values from Hulu Cave, Yangzi Cave and Bittoo Cave suddenly decreased by $3.2\text{\textperthousand}$, $1.7\text{\textperthousand}$ and $7.5\text{\textperthousand}$ respectively, indicating the synchronous strengthen of EASM and ISM (Figs. 4 and 5). On the other hand, the change of stalagmite $\delta^{18}\text{O}$ in the ISM region

displayed larger amplitudes than that in YZ1 $\delta^{18}\text{O}$ records (e.g., during H events, the average amplitude of $\delta^{18}\text{O}$ changes in Bittoo Cave is $\sim 5\text{\textperthousand}$, which is only $\sim 1.5\text{\textperthousand}$ in YZ1 records) (Fig. 5C and D).

The variations of ISM and EASM was obviously synchronous on orbital timescale, too. During the transition from MIS3 to MIS2, following the decrease of NHSI, the “stepped” increasing of $\delta^{18}\text{O}$ values in YZ1 (discussed in 4.2.5), is similar to the changes in the ISM records (Fig. 5). ISM intensity started to decline in the middle stage of MIS3, and the abrupt change occurred at the beginning of H1 (~16 ka BP). This abrupt declination of ISM was clearly revealed by a $6.3\text{\textperthousand}$ increasing of stalagmite $\delta^{18}\text{O}$ in Bittoo Cave (Kathayat et al., 2016) (Fig. 5D). In addition, both the ISM and EASM directly responded to the changes of NHSI in MIS5a (Fig. 7C–E).

The change of ISM, inferred from stalagmites, peat, and pollen records in Southwest China, was decoupled or reversed with EASM during the last deglaciation and Holocene (Hong et al., 2014; Jiang et al., 2014; Huang et al., 2016). Although some researches also demonstrated that there was a significant lag between the NHSI maxima and the response of ISM (Clemens and Prell, 2003; Bolton et al., 2013). Multi-mechanisms have been proposed to explain the differences between ISM and EASM, including the different monsoon systems internal feedback mechanisms (Jiang et al., 2017), the thermal condition in the equatorial Pacific (Hong et al., 2014), the difference of the magnitude and direction of the ITCZ shift over the Indian subcontinent and East Asia (Hong et al., 2019), and changes in atmospheric circulation and moisture trajectories (Maher and Thompson, 2012; Tan, 2014). While, the synchronous climatic changes in the ISM, EASM, high-latitudes and low-latitudes indicated that both the climatic changes in the high and low latitudes plays an important role in controlling the in-phase changes of the EASM and ISM (Figs. 4, Fig. 5, Fig. 7) (Deplazes et al., 2013; Kathayat et al., 2016; Nair et al., 2019; Sun et al., 2019).

4.2.3. Influence of Antarctic temperature change on the ASM

Although the change of ASM inferred from stalagmite records was consistent with climate change in the North Atlantic and

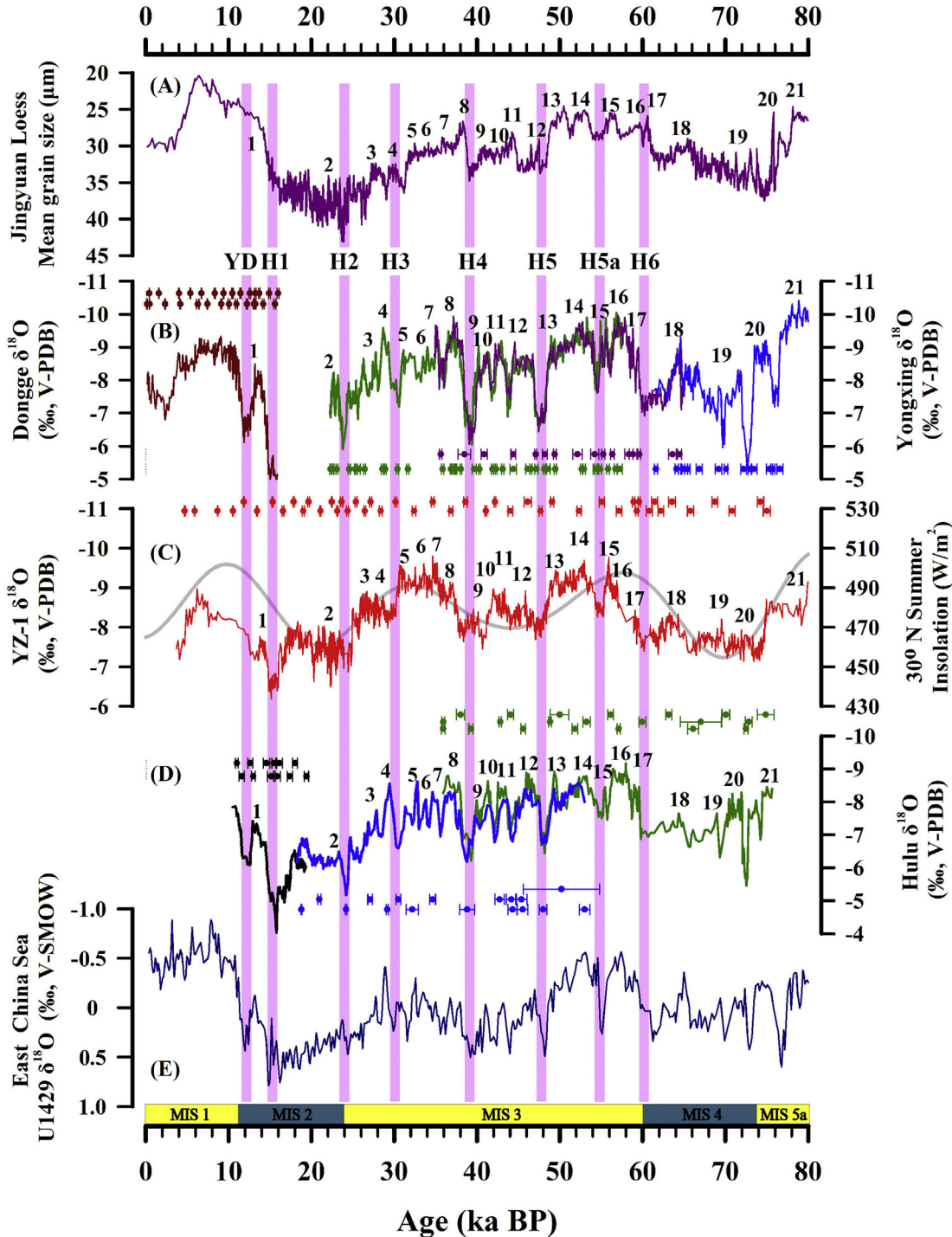


Fig. 4. The last glacial YZ1 $\delta^{18}\text{O}$ record compared with the climatic records in the Asian monsoon region. (A) Jingyuan Loess mean grain size (Sun et al., 2010); (B) Dongge Cave (Yuan et al., 2004) and Yongxing Cave (Chen et al., 2016) stalagmites $\delta^{18}\text{O}$ records (dark red curves indicate Dongge D4 stalagmite, green, purple and blue curves show Yongxing YX51, YX55, and YX46 stalagmite, respectively); (C) The red curve indicates the YZ1 stalagmite $\delta^{18}\text{O}$ record (this study) and the gray curve shows the 30 °N summer insolation (Berger and Loutre, 1991); (D) Hulu Cave stalagmites $\delta^{18}\text{O}$ records (Wang et al., 2001) (black, blue and green curves represent PD, MSD, and MLS stalagmite, respectively); (E) International Ocean Discovery Program sediment cores U1429 $\delta^{18}\text{O}$ record (Clemens et al., 2018). The corresponding age control points and age errors of each stalagmite record are expressed by corresponding colors. The pink vertical bars indicate YD and H events (Heinrich, 1988); the numbers indicate the D-O event (Dansgaard et al., 1993). (For interpretation of the references to color in this figure legend, the reader is referred to the Web version of this article.)

Greenland, some studies also demonstrated the potential correlation between ASM and climate change in the Antarctic (Cai et al., 2006; Han et al., 2016; Zhang et al., 2017). Comparison between YZ1 $\delta^{18}\text{O}$ records and Antarctic ice core records indicated that at millennium timescale, the weakening of ASM intensity

corresponded to the warm event in Antarctic, even with the similar duration and trend (Fig. S2).

In the boreal summer, heat and moisture were transported from the Southern equator-tropical Indian Ocean and Pacific Ocean to the Asian monsoon regions (Zhu, 2012; Ding et al., 2018), and the

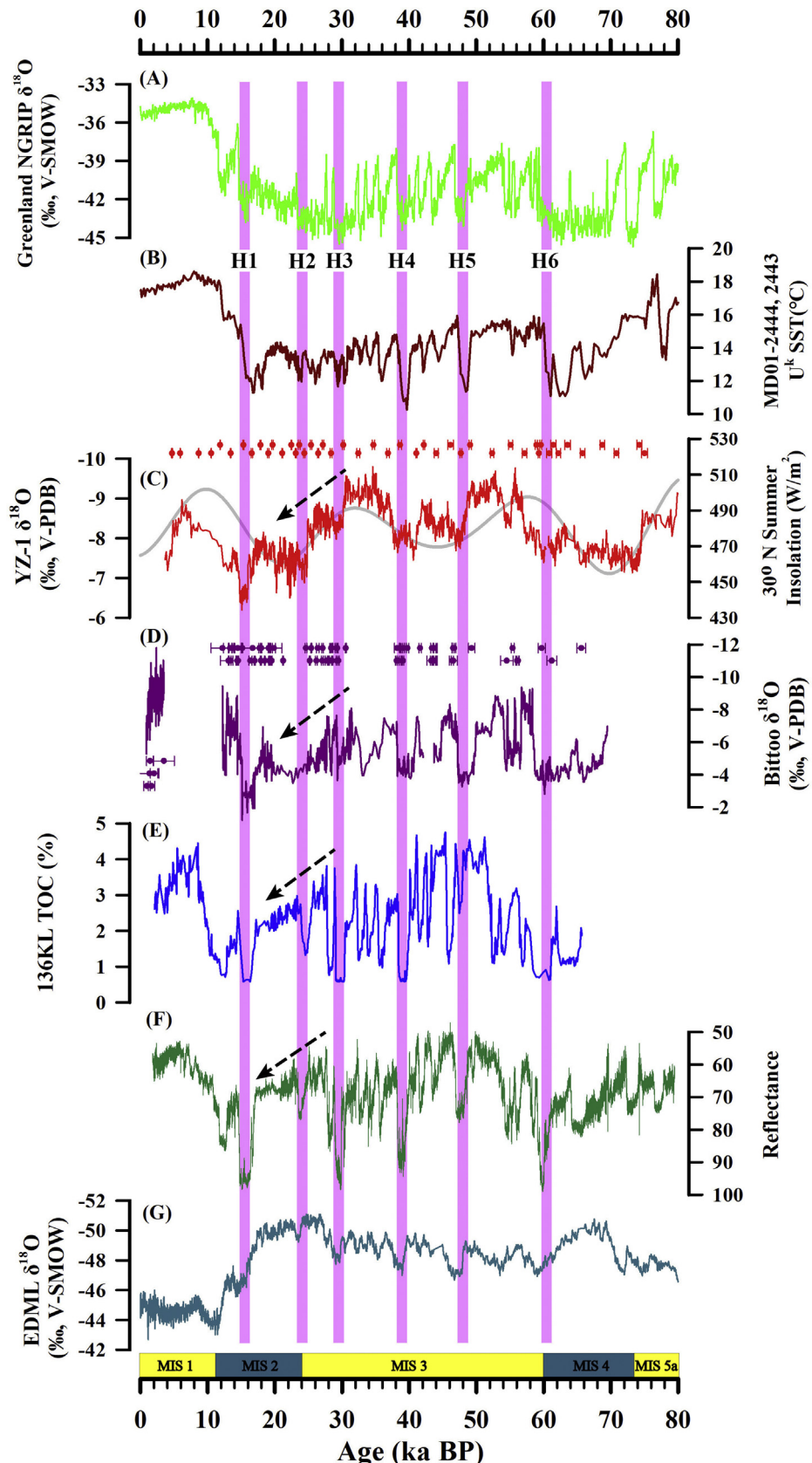


Fig. 5. (A) NGRIP ice core $\delta^{18}\text{O}$ record (NGRIP Members, 2004); (B) Sea surface temperature change records reconstructed from the Iberian margin marine sediment cores MD01-2444 and MD01-2443 (Belen et al., 2007); (C) YZ1 stalagmite $\delta^{18}\text{O}$ record (This study). The gray curve shows the 30°N summer insolation (Berger and Loutre, 1991); (D) Bittoo Cave stalagmites $\delta^{18}\text{O}$ records (Kathayat et al., 2016); (E) Arabian Sea sediment cores S90-136 KL TOC record (Schulz et al., 1998); (F) Arabian Sea sediment cores SO130-289 KL reflectance record (Deplazes et al., 2013); (G) Antarctic EDML ice core $\delta^{18}\text{O}$ record (EPICA Community Members, 2006); The pink vertical bars indicate YD and H events (Heinrich, 1988). (For interpretation of the references to color in this figure legend, the reader is referred to the Web version of this article.)

whole process was regulated by the ice volume and temperature in SH at glacial-interglacial timescale (Nair et al., 2019). The cross-equatorial low-level flow of the Somali Jet, originating from the South Indian Ocean, is the main channel for the transportation of water vapor to the ASM. In this process, the climate change signal from the SH was transmitted to the Asian monsoon region (Chen et al., 2016; Ding et al., 2018) (Fig. S3). Mascarene High plays a leading role in the climate interactions between the Northern and Southern hemispheres, and also between the Indian Ocean and its surrounding areas (Nair et al., 2019).

Furthermore, the reflectance records from marine cores in the Arabian Sea indicated the changes in the marine productivity and the intensity of Indian summer monsoon (ISM) (Deplazes et al., 2013). Comparison between the YZ1 $\delta^{18}\text{O}$ and the Arabian Sea reflectance records also demonstrated that both records exhibit fluctuations at millennial timescale during the last glacial period, and the increase of the Arabian Sea marine productivity was consistent with the strengthening of ASM, corresponding to the decrease of temperature in the Antarctic region (Fig. 5F).

The decrease of temperature in the Antarctic resulted in the strengthen of the Mascarene High, Somali Jet and northward cross-equatorial airflows (Fig. S2; Fig. S3), and finally strengthened the intensity of the ISM and the marine productivity of the Arabian Sea (Fig. 5F), taking more abundant precipitation to the Asian monsoon region (Fig. 6A) (Mcgee et al., 2014; An et al., 2015). The Mascarene High acted as a bridge in delivering the climate signal of Antarctic to EASM. Our records further proved that during the last glacial period, temperature changes in Antarctica were responded by ASM (Han et al., 2016; Zhang et al., 2017; Nair et al., 2019), and atmospheric circulations played a key role in transmitting signals of climate change.

4.2.4. Weakening of ASM during MIS 5d

Weakening of ASM intensity during MIS 5d was one of the most significant features in all the stalagmites recorded from the Asian monsoon region (Fig. 7). A similar decline of summer monsoon has also been demonstrated in Chinese Loess and the marine core from the East China Sea (Fig. 7B, F). The very weak ASM during MIS 5d did not correspond to a homologous cooling in the NGRIP records

(Fig. 7A), indicating that the main reason for this weak ASM during MIS 5d may not initiate from the high latitudes of the NH. In the case of relative low ice volume during MIS 5d (Fig. 7G), the ASM system may operate relatively independently, and mainly responding to the changes in summer solar insolation (Fig. 7C and D) (Beck et al., 2018).

In Sanbao, Dongge and other caves (Fig. 1), the $\delta^{18}\text{O}$ values during MIS 5d and MIS 2 were approximately the same ($\sim 6.2\text{\textperthousand}$) (Fig. 7D). The change of precipitation in the East China Sea and the runoff of the Yangtze River valley also showed miniature difference between MIS 5d and MIS 2 ($<0.2\text{\textperthousand}$) (Fig. 7F). Nevertheless, the YZ1 $\delta^{18}\text{O}$ in MIS 5d is nearly $1.5\text{\textperthousand}$ higher than that in MIS 2 (Fig. 7C), which is significantly different from other stalagmite records in the East Asian monsoon region.

Firstly, the changes of the $\delta^{18}\text{O}$ of moisture source vapor may provide an explanation for the special higher $\delta^{18}\text{O}$ values of YZ1 in MIS 5d. Previous analyses of modern precipitation in the ISM and EASM regions has shown that the $\delta^{18}\text{O}$ and δD compositions of the moisture sources for the ISM and EASM were essentially different (Tan, 2014; Cai et al., 2017; Li et al., 2017). The Indian Ocean is the dominant source of water vapor for the ASM, and the changes in sea surface temperature (SST) and moisture export in the Indian Ocean have an important impact on the precipitation $\delta^{18}\text{O}$ of the ASM (Baker et al., 2015; Yang et al., 2016). As a typical tropical monsoon, the ISM is driven by insolation-induced sensible heating, and the climate changes in low latitudes presented the precession cycles most significantly (Loutre et al., 2004). Decreased NHSI and induced southward movement of ITCZ weakened the convective activity over the tropical Indian Ocean, leading to significantly higher $\delta^{18}\text{O}$ of ASM precipitation in the downstream area (Yang et al., 2016; Cai et al., 2018; Ruan et al., 2019). The $\delta^{18}\text{O}$ of stalagmite YZ1 recorded the highest value ($-4.8\text{\textperthousand}$) during MIS 5d, which was well consistent with the weakest NHSI since 120 ka BP (Fig. 7C). In addition, the Indian monsoon, originates from the trade winds traversing the equator from the southern tropical ocean, was better than the East Asian monsoon in northward transmitting precession signals from tropical regions (Han et al., 2010). The combination of these factors lead to the water vapor transported to China was isotopically enriched during the period of low NHSI, and preserved

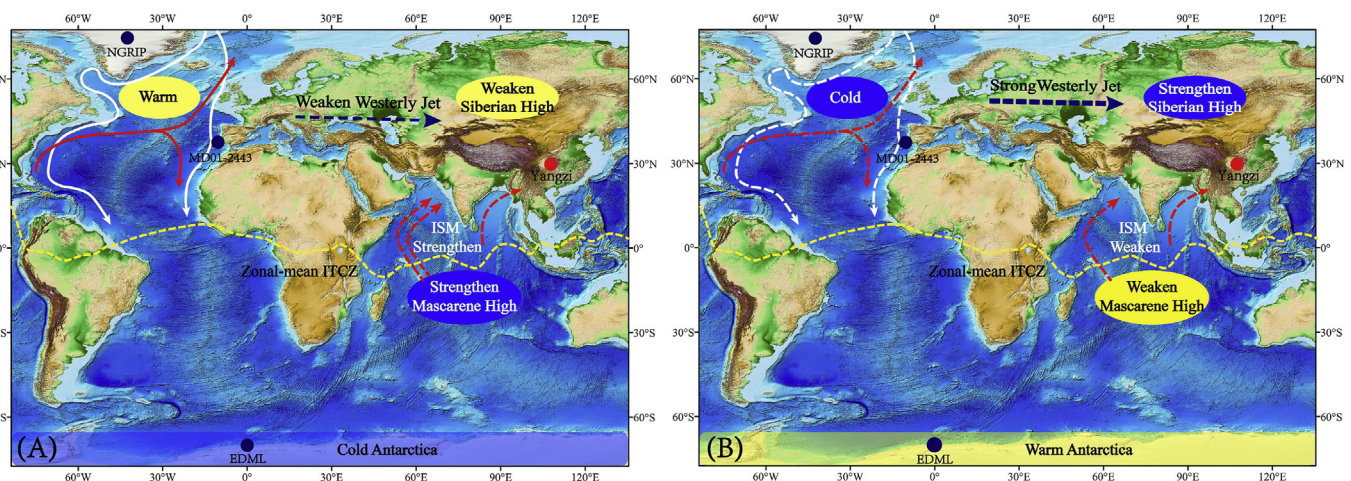


Fig. 6. The influence of Antarctic temperature and Mascarene High on the Asian monsoon. (A) The influence of a cold phase of Antarctic temperature and the strengthening Mascarene High on the ASM. (B) The influence of Antarctic warming and weakening Mascarene High on the ASM. Red and white arrows show warm Atlantic inflow to the Nordic Seas and main bottom current pathways in the North Atlantic (Muschiello et al., 2019). The blue arrow indicates the Westerly Jet in the NH. The yellow dashed lines denote the zonal-mean position of the ITCZ (Mcgee et al., 2014). The red dotted arrows indicate Indian summer monsoon (ISM). Blue dots are NGRIP ice core (NGRIP Members, 2004), Iberia marginal sea sediment cores MD01-2444 and MD01-2443 (Belen et al., 2007), and Antarctic EDML ice core (EPICA Community Members, 2006) respectively. The red dot represents Yangzi cave (This study). The base map is from <https://www.ngdc.noaa.gov/mgg/global/>. (For interpretation of the references to color in this figure legend, the reader is referred to the Web version of this article.)

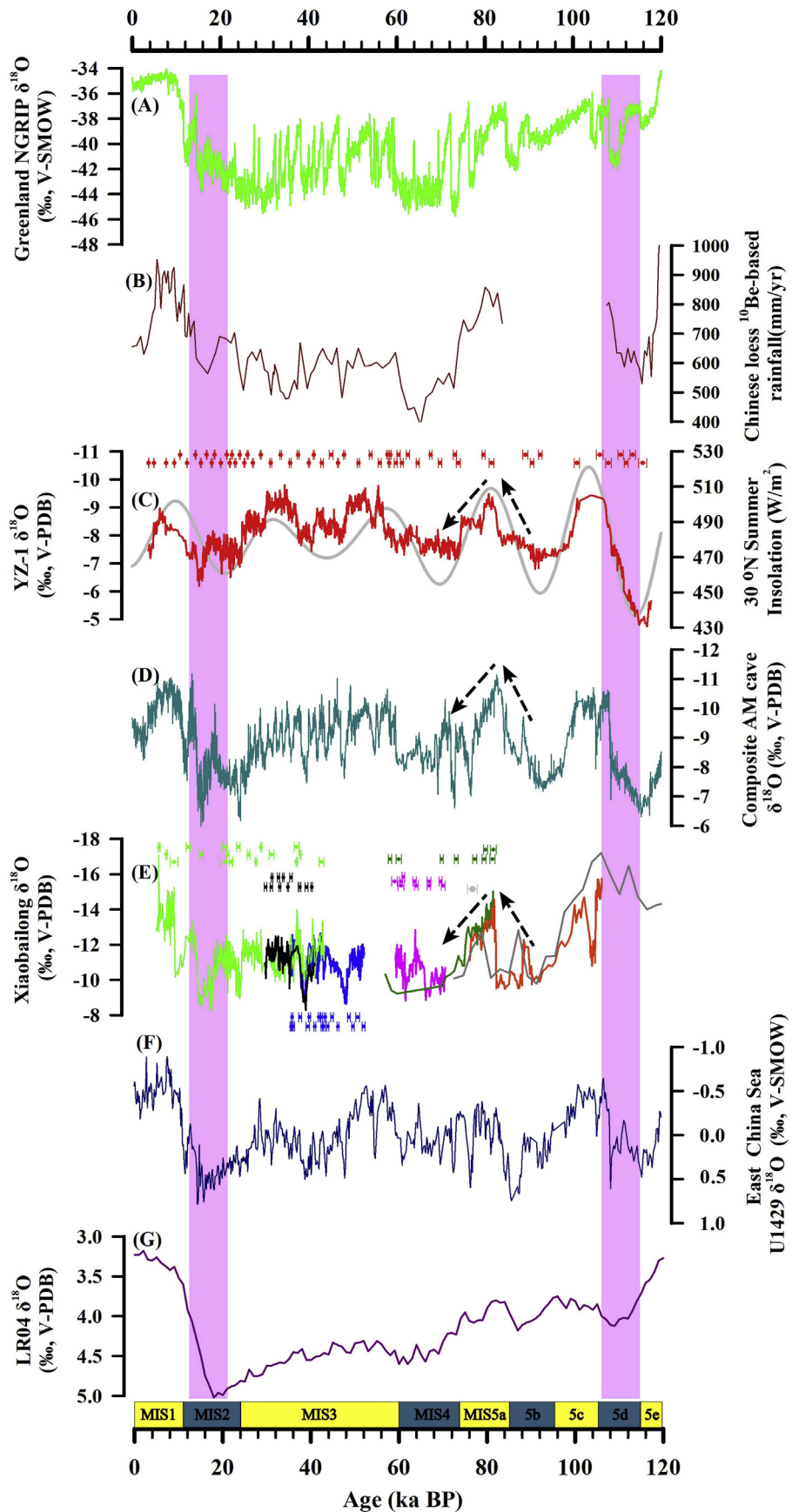


Fig. 7. (A) NGRIP ice core $\delta^{18}\text{O}$ record (NGRIP Members, 2004); (B) EASM Precipitation Record based on ^{10}Be reconstruction in Chinese loess (Beck et al., 2018); (C) The red curve indicates the YZ1 stalagmite $\delta^{18}\text{O}$ record (this study), the gray curve shows 30°N summer insolation (Berger and Loutre, 1991); (D) Composite Chinese cave speleothem $\delta^{18}\text{O}$ record (Cheng et al., 2016); (E) Xiaobailong Cave $\delta^{18}\text{O}$ record (Cai et al., 2015); (F) International Ocean Discovery Program sediment cores U1429 $\delta^{18}\text{O}$ record (Clemens et al., 2018); (G) Global stack benthic foraminifer $\delta^{18}\text{O}$ sequence LR04 (Lisicki and Raymo, 2005). The purple bands represent MIS 2 and MIS 5d, respectively. (For interpretation of the references to color in this figure legend, the reader is referred to the Web version of this article.)

in the speleothem records.

Secondly, Yangzi cave is located in the boundary area between ISM and EASM, which may reflect the monsoon dynamics between ISM and EASM induced by the change of NHSI. The changes in solar insolation on orbital timescale lead to anti-phase changes in Indian Ocean trade winds and North Pacific trade winds, which driven by Southern Indian Ocean subtropical high (SISH) and North Pacific subtropical high (NPSH), respectively (Walker et al., 2015). There is an “intertropical seesaw” between the tropical Hadley and Walker circulations, which influencing on the EASM intensity and the variation of stalagmite $\delta^{18}\text{O}$, by regulating the proportions of water vapor transported by the ISM and the Western North Pacific summer monsoon to the East Asian monsoon region (Maher and Thompson, 2012; Tan, 2014; Beck et al., 2018). When boreal summer isolation was in minima during MIS 5d, the warmer SST in the South Indian ocean and weaker Southern Hadley circulation, result in weakening trade winds and Somali jet in the Indian ocean, eventually weakening the ISM (Beck et al., 2018; Nair et al., 2019). Simulations based on LGM boundary conditions also suggested that during LGM the precipitation decreased significantly over the Indian Ocean and Indian subcontinent, and the precipitation $\delta^{18}\text{O}$ increased by about 2‰–4‰ (Cai et al., 2015). However, precipitation has increased in East Asia during the LGM, and the precipitation $\delta^{18}\text{O}$ showed either minor increases or decreases of 1.0‰–2.0‰ (Cai et al., 2015). In addition, the sea level during MIS 2 was lower than that in MIS 5d (Fig. 7G) (Lisiecki and Raymo, 2005). The exposure of continental shelf associated with a lower sea level condition can alters regional hydrologic pattern in Southeast Asia (DiNezio and Tierney, 2013), increasing the distance from water vapor source to the monsoon region, and finally resulting in more negative $\delta^{18}\text{O}$ in precipitation (Li et al., 2014). Based on the above discussions, the more positive $\delta^{18}\text{O}$ values during MIS 5d with low NHSI may be induced by the changes of the $\delta^{18}\text{O}$ of moisture source and the dynamic changes of monsoon circulations.

4.2.5. Stepped changes of YZ1 $\delta^{18}\text{O}$ during MIS 3 and MIS 5

Another significant feature in the variation of YZ1 $\delta^{18}\text{O}$ is the stepped bias during the period of MIS 3 and MIS 5a, corresponding to the change of NHSI from maximum to minimum (Figs. 3 and 7C). Specifically, in MIS 5a, from D/O 22 to 20, with the NHSI from 510 to 455 (W/m^2), the stalagmite $\delta^{18}\text{O}$ values changed from –9.5‰ (D/O 22) to –8.5‰ (D/O 21), and finally to –7‰ (D/O 20) (Fig. 3). Similar stepped bias in the change of YZ1 $\delta^{18}\text{O}$ were also presented from D/O 13–16 to D/O 10–12, and to D/O 9; and from D/O 5–8 to D/O 3–4, and to D/O 2 in the late MIS 3, the overall variation of $\delta^{18}\text{O}$ is about 4‰ (Fig. 3).

Tropical oceans are one of the essential drivers of modern monsoon, as well as the source of heat and moisture in the Global Monsoon system (Wang et al., 2017). During MIS 3 and MIS 5a, under the background of increasing global ice volume (Fig. 7G), the ASM continuously weakened after the maximum of NHSI (after D/O 8–5 in MIS 3 and D/O 22 in MIS 5a) (Fig. 7C), and cannot recover to its previous level because of the gradual weakening of NHSI (Figs. 3 and 7C). Other paleoclimatic records in the Asian monsoon region were also characterized by frequent fluctuations during MIS 3 and MIS 5 (Figs. 4 and 7), indicating the instability of ASM intensity in the Asian monsoon regions in this period (Sun et al., 2010; Chen et al., 2016). These phenomena confirmed the co-regulation to ASM by global ice volume and NHSI at millennium and orbital time scales.

4.3. Climate and environmental significance of $\delta^{13}\text{C}$

4.3.1. Covariation between YZ1 $\delta^{18}\text{O}$ and $\delta^{13}\text{C}$

The positive correlation between the speleothem $\delta^{18}\text{O}$ and $\delta^{13}\text{C}$

along the growth axis had been considered to be an indicator of kinetic effects for the fractionation of stable isotopes, and these speleothem samples should be excluded to the reconstruction of paleoclimate (Hendy, 1971). In recent years, however, the validity of Hendy test has been argued (Fairchild et al., 2006; Dorale and Liu, 2009). The Hendy test is not a sufficient condition for test whether oxygen and carbon isotopes are kinetically disturbed (Mickler et al., 2004), and it is difficult to prove that stalagmites are completely deposited in equilibrium fractionation on orbital scale.

The kinetic effects on cave precipitates is common phenomenon (Mickler et al., 2006), especially on short timescales. Even if kinetic effects existed, the climate signals contained by $\delta^{13}\text{C}$ will not be masked completely (McDermott, 2004; Fairchild et al., 2006; Cosford et al., 2009; Liu et al., 2016). Model simulation results show that when the humidity is more than 85%, the changes of humidity and ventilation is less than 5% and 0.1 m/s respectively (equivalent to stable cave environment), the change of calcite oxygen and carbon isotopes caused by evaporation can be neglected (Deininger et al., 2012; Dreybrodt and Deininger, 2014).

In addition, oxygen and carbon isotopes of stalagmites have covariation characteristics on the century - millennium scale which has been confirmed in the stalagmite records of South China (Cosford et al., 2009; Kuo et al., 2011; Liu et al., 2016; Zhang et al., 2019), indicating that it is not a special phenomenon. There is a significant positive correlation ($r = 0.47$, $P < 0.01$) between the detrended $\delta^{13}\text{C}$ and $\delta^{18}\text{O}$ data of stalagmite YZ1 (Fig. S4). Further cross-wavelet analysis of $\delta^{13}\text{C}$ and $\delta^{18}\text{O}$ shows that both of them have the same cycle on the orbital-millennium scale (Fig. S5). The strong covariance between the $\delta^{13}\text{C}$ and $\delta^{18}\text{O}$ values of stalagmite YZ1 on orbital scale should be attributed to climate and hydrological conditions, even the absolute amplitude for the variation of $\delta^{13}\text{C}$ and $\delta^{18}\text{O}$ are potentially amplified by kinetic effects.

4.3.2. $\delta^{13}\text{C}$ records of stalagmite YZ1 and regional hydrology

Weak summer monsoons in periods MIS 2, MIS 4, MIS 5b, and MIS 5d corresponded to higher $\delta^{13}\text{C}$ values (Fig. 3). Particularly in the interval of 110–117 ka BP, the significant weakening of NHSI and ASM resulted in the distinct degradation of regional ecological environment and significant decrease of biological activity, which was recorded by the highest values of YZ1 $\delta^{13}\text{C}$ (Fig. 3). In addition, the ASM intensity of MIS 2 was weaker than that of MIS 4, and also responded by $\delta^{13}\text{C}$ values. The average value of $\delta^{13}\text{C}$ in MIS 2 was –8.9‰, higher than that of –9.7‰ in MIS 4.

On the centennial – millennial scales, e.g. at 24.7 and 20.1 ka BP, there were two abrupt positive excursions of $\delta^{13}\text{C}$ values with amplitude of 3.5‰ and 2.9‰ respectively (Fig. 3), consistent with the weakening of ASM and indicated the suddenly declination of local ecological conditions and biologic-CO₂ production.

On the orbital – millennial scales, during 62–57 ka BP and 24–10 ka BP, the $\delta^{13}\text{C}$ values were negatively changed significantly (with the amplitude of 3.7‰ and 3.3‰ respectively), corresponding to the transition from MIS 4 to MIS 3 (the end of H6) and from MIS 2 to MIS 1 (the end of the LGM to the Holocene), respectively (Fig. 3B). These changes indicated that under the background of decreasing global ice volume (Fig. 7G) and strengthening ASM (Fig. 3A), the precipitation increased, local hydrological conditions have ameliorated, and biologic-CO₂ yield was enhanced in this area. By contrast, the ~3‰ and ~5‰ positive excursions of $\delta^{13}\text{C}$ values at 74 ka BP – 65 ka BP and 32 ka BP – 26 ka BP, corresponding to the transition of MIS 5a to MIS 4 and MIS 3 to MIS 2 respectively, consistent with the ~2–~4‰ positive change of $\delta^{18}\text{O}$ (Fig. 3).

4.3.3. Coupling of stalagmite $\delta^{18}\text{O}$ and $\delta^{13}\text{C}$

In the period of 82–74 ka BP (in MIS 5a), with the decrease of NHSI, YZ1 $\delta^{18}\text{O}$ abruptly increased ~2‰ at 79.9 ka BP (D/O 22 to 21)

and 74.7 ka BP (D/O 21 to 20) (Fig. 3A). At the same time, there was no abrupt change in the variation of $\delta^{13}\text{C}$ values changes. Although both of the $\delta^{18}\text{O}$ and $\delta^{13}\text{C}$ values demonstrated a positive trend in this period, the $\delta^{13}\text{C}$ values were maintained at a relative negative level of $<-10\text{\textperthousand}$ (Fig. 3B). This may be attributed to the following factors: (1) During this period, the ASM tended to weaken, but maintained a relative high intensity overall (YZ stalagmite $\delta^{18}\text{O}$ was slightly lower than the average value) (Fig. 3A); (2) Although NBSI tended to decrease, the mean value was higher than that of MIS 3 and MIS 2 (Fig. 3A). Therefore, moderate precipitation and NBSI led to small decrease of the biologic- CO_2 yield and gradually positive change of YZ1 $\delta^{13}\text{C}$. It is plausible that the change of local hydrological conditions and biological activity are not only controlled by precipitation, but also by the intensity of solar insolation (which affects regional temperature and evaporation), and ultimately dominate the regional effective humidity (Li et al., 2018). In MIS 3, the ASM fluctuated around a strong level (Fig. 3A), and the changes of $\delta^{13}\text{C}$ values demonstrated a similar pattern and maintained at a relative lower level ($<-10\text{\textperthousand}$) (Fig. 3B), indicating better local ecological environment during MIS 3 than that of MIS 4. Furthermore, during the period of D/O 9–12, although the ASM weakened, the local ecological environment indicated by $\delta^{13}\text{C}$ did not deteriorate significantly (Fig. 3B). It can be attributed to the low NBSI and weakening regional evaporation during this period, which did not result in essential deterioration of regional hydrological conditions and effective humidity.

During the LGM in MIS 2, with the lowest global temperature since the last glacial period (Bond et al., 1993; Dansgaard et al., 1993), the $\delta^{18}\text{O}$ values of stalagmite YZ1 changed positively and gradually (Fig. 3A). However, the variation of $\delta^{13}\text{C}$ during 24–22 ka BP and 20–16 ka BP was opposite to that of $\delta^{18}\text{O}$, showing a trend of gradually lowering. For example, the $\delta^{13}\text{C}$ value during H 1 was $\sim 9.5\text{\textperthousand}$, lower than that of $\sim 8.0\text{\textperthousand}$ in H 2 (Fig. 3). During the LGM, the annual average temperature in the low latitudes of South China decreased by about 4–6 °C (Wang et al., 2012; Xue et al., 2015). Although the vegetation density decreased, C3 vegetation was still dominant (Li et al., 2013). Despite the decrease in temperature and precipitation, the NBSI and regional evaporation were also decreased, resulting a stable humid climate in South China (He et al., 2015; Li et al., 2018). Therefore, during H1, although the ASM weakened, the regional evaporation might be declined due to the lower temperature. Finally, the regional hydrological conditions might not have changed appreciably. The moderate climate did not lead to significant decrease in soil biomass and biologic- CO_2 yield. So, the change of $\delta^{13}\text{C}$ values of stalagmite YZ1 showed a significant reverse trend to that of the $\delta^{18}\text{O}$ in H 2 and H 1 (Fig. 3).

5. Conclusions

Based on high-precise ^{230}Th dating and coupled $\delta^{18}\text{O}$ and $\delta^{13}\text{C}$ analyses, a stalagmite records from Yangzi Cave, southwestern China, has been used to reconstruct the evolution of ASM and regional hydrological conditions since the Last Interglacial period (3.6–118.1 ka BP). Systematic comparisons indicate that there is a synchronous relationship between the ISM and EASM on millennial and orbital timescales, revealed by a series of abrupt millennial climate events during the last glacial period, such as YD, D/O, and H events. Both the ISM and EASM were influenced by the climate change in the NH high latitudes and the large-scale atmospheric circulations dominated by NBSI. Climate change in the SH high-latitudes can influence on the change of ASM through the Mascarene High and the Somali Jet.

The $\delta^{18}\text{O}$ values of stalagmite YZ1 in MIS 5d is nearly 1.5% higher than that in the Maximum of last glacial period (MIS 2). This significant positive excursion of $\delta^{18}\text{O}$ values responded to the

decreasing NBSI, and closely related weakening of ISM intensity and convective activity, which finally lead to the changes of $\delta^{18}\text{O}$ in moisture source and the dynamic of monsoon circulations.

Variations in stalagmite $\delta^{13}\text{C}$ reflected the changes of regional ecological environment under the control of ASM. The NBSI and ASM ultimately determined the change of stalagmite $\delta^{13}\text{C}$ by influencing on regional hydrological conditions and biological activity. Our research further showed that the strong covariation characteristic of YZ1 $\delta^{13}\text{C}$ and $\delta^{18}\text{O}$ was resulted by the common driving factors. The combination of stalagmite $\delta^{13}\text{C}$ and $\delta^{18}\text{O}$ is suitable in the reconstruction of paleoclimate and paleoenvironment.

Declaration of competing interest

The authors declare no conflict of Interest.

CRediT authorship contribution statement

Yao Wu: Writing - original draft. **Ting-Yong Li:** Conceptualization, Project administration, Funding acquisition, Writing - review & editing. **Chao-Jun Chen:** Data curation, Formal analysis. **Jian Zhang:** Data curation, Formal analysis. **Jun-Yun Li:** Data curation, Formal analysis. **Tao Wang:** Data curation, Formal analysis. **Ran Huang:** Data curation, Formal analysis. **Si-Ya Xiao:** Data curation, Formal analysis.

Acknowledgments

This research was supported by National Natural Science Foundation of China (NSFC, No. 41772170, 4191101278), the State Cultivation Base of Eco-agriculture for Southwest Mountainous Land, Southwest University, China (No. 5330200076), and the Fundamental Research Funds for the Central Universities, China (No. XDKJ2017A010) to T.-Y Li; U-Th dating was supported by the Science Vanguard Research Program of the Ministry of Science and Technology (108-2119-M-002-012 to C.-C.S.), the National Taiwan University (105R7625 to C.-C.S.), and the Higher Education Sprout Project of the Ministry of Education (108L901001 to C.-C.S.). Professor Ian. J. Fairchild, University of Birmingham, U.K., is greatly appreciated for improving the science of this MS and polishing the MS thoroughly. Great thanks to Editor Dr. Ana Moreno and two anonymous reviewers for their comments and suggestions.

Appendix A. Supplementary data

Supplementary data to this article can be found online at <https://doi.org/10.1016/j.quascirev.2020.106261>.

References

- An, Z.S., Wu, G.X., Li, J.P., Sun, Y.B., Liu, Y.M., Zhou, W.J., Cai, Y.J., Duan, A.M., Li, L., Mao, J.Y., Cheng, H., Shi, Z.G., Tan, L.C., Yan, H., Ao, H., Chang, H., Feng, J., 2015. Global monsoon dynamics and climate change. In: Jeanloz, R., Freeman, K.H. (Eds.), Annual Review of Earth and Planetary Sciences, pp. 29–77.
- Baker, A.J., Sodemann, H., Baldini, J.U.L., Breitenbach, S.F.M., Johnson, K.R., van Hunen, J., Zhang, P., 2015. Seasonality of westerly moisture transport in the East Asian summer monsoon and its implications for interpreting precipitation $\delta^{18}\text{O}$. *J. Geophys. Res.: Atmos.* 120, 5850–5862.
- Bar-Matthews, M., Ayalon, A., Kaufman, A., 1997. Late quaternary paleoclimate in the eastern Mediterranean region from stable isotope analysis of speleothems at soreq cave, Israel. *Quat. Res.* 47, 155–168.
- Beck, J.W., Zhou, W.J., Li, C., Wu, Z.K., White, L., Xian, F., Kong, X.H., An, Z.S., 2018. A 550,000-year record of East Asian monsoon rainfall from ^{10}Be in loess. *Nature* 360, 877–881.
- Belen, M., Grimalt, J.O., Shackleton, N.J., Lucia, D.A., Hutterli, M.A., Stocker, T.F., 2007. Four climate cycles of recurring deep and surface water destabilizations on the Iberian margin. *Science* 317, 502–507.
- Berger, A., Loutre, M., 1991. Insolation values for the climate of the last 10 million

- years. *Quat. Sci. Rev.* 10, 297–317.
- Bolton, C.T., Chang, L., Clemens, S.C., Kodama, K., Ikebara, M., Medina-Elizalde, M., Paterson, G.A., Roberts, A.P., Rohling, E.J., Yamamoto, Y., Zhao, X., 2013. A 500,000 year record of Indian summer monsoon dynamics recorded by eastern equatorial Indian Ocean upper water-column structure. *Quat. Sci. Rev.* 77, 167–180.
- Bond, G., Broecker, W., Johnsen, S., McManus, J., Labeyrie, L., Jouzel, J., Bonani, G., 1993. Correlations between climate records from North Atlantic sediments and Greenland ice. *Nature* 365, 143–147.
- Cai, Y.J., An, Z.S., Cheng, H., Edwards, R.L., Kelly, M.J., Liu, W.G., Wang, X.F., Shen, C.C., 2006. High resolution absolute-dated Indian monsoon record between 53 and 36 ka from xiaobailong cave, Southwestern China. *Geology* 34, 621–624.
- Cai, Y.J., Fung, I.Y., Edwards, R.L., An, Z.S., Cheng, H., Lee, J.-E., Tan, L.C., Shen, C.C., Wang, X.F., Day, J.A., Zhou, W.J., Kelly, M.J., Chiang, J.C.H., 2015. Variability of stalagmite-inferred Indian monsoon precipitation over the past 252,000 y. *Proc. Natl. Acad. Sci. Unit. States Am.* 112, 2954–2959.
- Cai, Z.Y., Tian, L.D., Bowen, G.J., 2017. ENSO variability reflected in precipitation oxygen isotopes across the Asian Summer Monsoon region. *Earth Planet Sci. Lett.* 475, 25–33.
- Cai, Z.Y., Tian, L.D., Bowen, G.J., 2018. Spatial-seasonal patterns reveal large-scale atmospheric controls on Asian Monsoon precipitation water isotope ratios. *Earth Planet Sci. Lett.* 503, 158–169.
- Chen, C.J., Li, T.-Y., 2018. Geochemical characteristics of cave drip water respond to ENSO based on a 6-year monitoring work in Yangkou Cave, Southwest China. *J. Hydrol.* 561, 896–907.
- Chen, S.T., Wang, Y.J., Cheng, H., Edwards, R.L., Wang, X.F., Kong, X.G., Liu, D.B., 2016. Strong coupling of Asian Monsoon and Antarctic climates on sub-orbital timescales. *Sci. Rep.* 6, 32995.
- Cheng, H., Edwards, R.L., Shen, C.C., Polyak, V.J., Asmerom, Y., Woodhead, J., Hellstrom, J., Wang, Y.J., Kong, X.G., Spotl, C., Wang, X.F., Alexander, E.C., 2013. Improvements in ^{230}Th dating, ^{230}Th - and ^{234}U -half-life values, and U-Th isotopic measurements by multi-collector inductively coupled plasma mass spectrometry. *Earth Planet Sci. Lett.* 371, 82–91.
- Cheng, H., Edwards, R.L., Sinha, A., Spotl, C., Yi, L., Chen, S.T., Kelly, M., Kathayat, G., Wang, X.F., Li, X.L., Kong, X.G., Wang, Y.J., Ning, Y.F., Zhang, H.W., 2016. Corrigendum: the Asian monsoon over the past 640,000 years and ice age terminations. *Nature* 534, 640–646.
- Clemens, S.C., Holbourn, A., Kubota, Y., Lee, K.E., Liu, Z., Chen, G., Nelson, A., Fox-Kemper, B., 2018. Precession-band variance missing from East Asian monsoon runoff. *Nat. Commun.* 9, 3364.
- Clemens, S.C., Prell, W.L., 2003. A 350,000 year summer-monsoon multi-proxy stack from the Owen ridge, northern Arabian Sea. *Mar. Geol.* 201, 35–51.
- Cosford, J., Qing, H.R., Matthey, D., Eglington, B., Zhang, M.L., 2009. Climatic and local effects on stalagmite $\delta^{13}\text{C}$ values at Lianhua Cave, China. *Palaeogeogr. Palaeoclimatol. Palaeoecol.* 280, 235–244.
- Dansgaard, W., Johnsen, S.J., Clausen, H.B., Dahl-Jensen, D., Gundestrup, N.S., Hammer, C.U., Hvidberg, C.S., Steffensen, J.P., Steimbjörnsdóttir, A.E., Jouzel, J., Bond, G., 1993. Evidence for general instability of past climate from a 250 kyr ice core record. *Nature* 364, 218–220.
- Deininger, M., Fohlmeister, J., Scholz, D., Mangini, A., 2012. Isotope disequilibrium effects: the influence of evaporation and ventilation effects on the carbon and oxygen isotope composition of speleothems – a model approach. *Geochem. Cosmochim. Acta* 96, 57–79.
- Deplazes, G., Lückge, A., Peterson, L.C., Timmermann, A., Hamann, Y., Hughen, K.A., Röhl, U., Laj, C., Cane, M.A., Sigman, D.M., Haug, G.H., 2013. Links between tropical rainfall and North Atlantic climate during the last glacial period. *Nat. Geosci.* 6, 213.
- DiNezio, P.N., Tierney, J.E., 2013. The effect of sea level on glacial Indo-Pacific climate. *Nat. Geosci.* 6, 485–491.
- Ding, Y.H., Si, D., Liu, Y.J., Wang, Z.Y., Li, Y., Zhao, L., Song, Y.F., 2018. On the characteristics, driving forces and inter-decadal variability of the East asian summer monsoon. *Chin. J. Atmos. Sci.* 42, 533–558.
- Dorale, J.A., Edwards, R.L., Ito, E., González, L.A., 1998. Climate and vegetation history of the midcontinent from 75 to 25 ka: a speleothem record from Crevice cave, Missouri, USA. *Science* 282, 1871–1874.
- Dorale, J.A., Liu, Z., 2009b. Limitations of hendy test carteria in judging the paleoclimatic suitability of speleothems and the need for replication. *J. Cave Karst Stud.* 71, 73–80.
- Dreybrodt, W., Deininger, M., 2014. The impact of evaporation to the isotope composition of DIC in calcite precipitating water films in equilibrium and kinetic fractionation models. *Geochem. Cosmochim. Acta* 125, 433–439.
- Dreybrodt, W., Scholz, D., 2011. Climatic dependence of stable carbon and oxygen isotope signals recorded in speleothems: from soil water to speleothem calcite. *Geochem. Cosmochim. Acta* 75, 734–752.
- EPICA Community Members, 2006. One-to-one coupling of glacial climate variability in Greenland and Antarctica. *Nature* 444, 195–198.
- Fairchild, I.J., Smith, C.L., Baker, A., Fuller, L., Spötl, C., Matthey, D., McDermott, F., EIMF, 2006. Modification and preservation of environmental signals in speleothems. *Earth Sci. Rev.* 75, 105–153.
- Feitmann, D., Cheng, H., Badertscher, S., Edwards, R.L., Mudelsee, M., Goekturk, O.M., Fankhauser, A., Pickering, R., Raible, C.C., Matter, A., Kramers, J., Tuysuz, O., 2009. Timing and climatic impact of Greenland interstadials recorded in stalagmites from northern Turkey. *Geophys. Res. Lett.* 36, L19707.
- Genty, D., Blamart, D., Ouahdi, R., Gilmour, M., Baker, A., Jouzel, J., Van-Exter, S., 2003. Precise dating of Dansgaard-Oeschger climate oscillations in western Europe from stalagmite data. *Nature* 421, 833–837.
- Han, L.-Y., Li, T.-Y., Cheng, H., Edwards, R.L., Shen, C.-C., Li, H.-C., Huang, C.-X., Li, J.-Y., Yuan, N., Wang, H.-B., Zhang, T.-T., Zhao, X., 2016. Potential influence of temperature changes in the Southern Hemisphere on the evolution of the Asian summer monsoon during the last glacial period. *Quat. Int.* 392, 239–250.
- Han, W.X., Fang, X.M., Yang, S.L., King, J., 2010. Differences between East Asian and Indian monsoon climate records during MIS3 attributed to differences in their driving mechanisms: evidence from the loess record in the Sichuan basin, Southwestern China and other continental and marine climate records. *Quat. Int.* 218, 94–103, 2018.
- He, Y.L., Zhao, C., Zheng, Z., Liu, Z.H., Wang, N., Li, J., Cheddadi, R., 2015. Peatland evolution and associated environmental changes in central China over the past 40,000 years. *Quat. Res.* 84, 255–261.
- Heinrich, H., 1988. Origin and consequences of cyclic ice rafting in the Northeast Atlantic Ocean during the past 130,000 years. *Quat. Res.* 29, 142–152.
- Hendy, C.H., 1971. The isotopic geochemistry of speleothems — I. The calculation of the effects of different modes of formation on the isotopic composition of speleothems and their applicability as paleoclimatic indicators. *Geochem. Cosmochim. Acta* 35, 801–824.
- Hong, B., Hong, Y.T., Uchida, M., Shibata, Y., Cai, C., Peng, H.J., Zhu, Y.X., Wang, Y., Yuan, L.G., 2014. Abrupt variations of Indian and East Asian summer monsoons during the last deglacial stadial and interstadial. *Quat. Sci. Rev.* 97, 58–70.
- Hong, B., Rabassa, J., Uchida, M., Hong, Y.T., Peng, H.J., Ding, H.W., Guo, Q., Yao, H., 2019. Response and feedback of the Indian summer monsoon and the Southern Westerly Winds to a temperature contrast between the hemispheres during the last glacial–interglacial transitional period. *Earth Sci. Rev.* 197, 102917.
- Huang, C., Wei, G.J., Ma, J.L., Liu, Y., 2016. Evolution of the Indian summer monsoon during the interval 32.7–11.4 cal. ka BP: evidence from the Baoxiu peat, Yunnan, southwest China. *J. Asian Earth Sci.* 131, 72–80.
- Jaffey, A.H., Flynn, K.F., Glendenin, L.E., Bentley, W.C., Essling, A.M., 1971. Precision measurement of half-lives and specific activities of ^{235}U and ^{238}U . *Phys. Rev. C* 4, 1889–1906.
- Jiang, X.Y., He, Y.Q., Shen, C.C., Lee, S.Y., Yang, B., Lin, K., Li, Z.Z., 2014. Decoupling of the East Asian summer monsoon and Indian summer monsoon between 20 and 17ka. *Quat. Res.* 82, 146–153.
- Jiang, X.Y., He, Y.Q., Wang, X.Y., Sun, X.S., Hong, H., Liu, J., Yu, T.L., Li, Z.Z., Shen, C.C., 2017. The preboreal-like asian monsoon climate in the early last interglacial period recorded from the dark cave, southwest China. *J. Asian Earth Sci.* 143, 39–44.
- Jouzel, J., Masson-Delmotte, V., Cattani, O., Dreyfus, G., Falourd, S., Hoffmann, G., Jouet, J., Barnola, J.M., Chappellaz, J., Fischer, H., Gallet, J.C., Johnsen, S., Leuenberger, M., Loulergue, L., Lüthi, D., Oerter, H., Parrenin, F., Raisbeck, G., Raynaud, D., Schwander, J., Spahni, R., Souchez, R., Selmo, E., Schilt, A., Steffensen, J.P., Stenni, B., Stauffer, B., Stocker, T., Tison, J.-L., Werner, M., Wolff, E.W., 2007. Orbital and millennial Antarctic climate variability over the last 800,000 years. *Science* 317, 793–796.
- Kathayat, G., Cheng, H., Sinha, A., Spotl, C., Edwards, R.L., Zhang, H.W., Li, X.L., Yi, L., Ning, Y.F., Cai, Y.J., Lui, W.L., Breitenbach, S.F.M., 2016. Indian monsoon variability on millennial-orbital timescales. *Sci. Rep.* 6, 24374.
- Kong, X.G., Wang, Y.J., Wu, J.Y., Cheng, H., Edwards, R.L., Wang, X.F., 2005. Complicated response of stalagmite $\delta^{13}\text{C}$ to climate change during the last glaciation from Hulu Cave, Nanjing, China. *Sci. China Earth Sci.* 48, 2174–2181.
- Kuo, T.S., Liu, Z.Q., Li, H.C., Wan, N.J., Shen, C.C., Ku, T.L., 2011. Climate and environmental changes during the past millennium in central western Guizhou, China as recorded by Stalagmite ZJD-21. *J. Asian Earth Sci.* 40, 1111–1120.
- Li, J., Zheng, Z., Huang, K.Y., Yang, S.X., Chase, B., Valsecchi, V., Carré, M., Cheddadi, R., 2013. Vegetation changes during the past 40,000 years in Central China from a long fossil record. *Quat. Int.* 310, 221–226.
- Li, T.-Y., Huang, C.-X., Tian, L., Suaraz, M.B., Gao, Y., 2018. Variation of $\delta^{13}\text{C}$ in plant-soil-cave systems in karst regions with different degrees of rocky desertification in Southwest China and implications for paleoenvironment reconstruction. *Journal of Cave and Karst Studies* 80 (4), 212–228. <https://doi.org/10.4311/2018ES0107>.
- Li, J.-Y., Li, T.-Y., 2018. Seasonal and annual changes in soil/cave air pCO_2 and the $\delta^{13}\text{C}_{\text{DIC}}$ of cave drip water in response to changes in temperature and rainfall. *Appl. Geochem.* 93, 984–101.
- Li, T.-Y., 2007. The Controlling Factors Research on the Paleoenvironmental Informations in Stalagmite and the Paleoclimate Reconstruction since the Last Glacial Period in Chongqing Area (D). Doctoral Dissertation of Southwest University, China, p. 10p (In Chinese).
- Li, T.-Y., 2018. False amount effect—a discussion on one issue of isotopic Climatology. *Quat. Sci.* 38 (2018), 1545–1548 (In Chinese).
- Li, T.-Y., Li, H.-C., Li, J.-Y., Yuan, D.-X., Wang, J.-L., Ye, M.-Y., Tang, L.-L., Shen, C.-C., Ye, C.-L., 2008. The $\delta^{13}\text{C}$ and $\delta^{18}\text{O}$ features and their significances speleothems in furong cave, Chongqing, China. *Geol. Rev.* 54, 712–720 (In Chinese).
- Li, T.-Y., Shen, C.-C., Li, H.-C., Li, J.-Y., Chiang, H.-W., Song, S.-R.L., Yuan, D.-X., Lin, C.-D.J., Gao, P., Zhou, L.-P., Wang, J.-L., Ye, M.-Y., Tang, L.-L., Xie, S.-Y., 2011. Oxygen and carbon isotopic systematics of aragonite speleothems and water in Furong Cave, Chongqing, China. *Geochem. Cosmochim. Acta* 75 (2011), 4140–4156.
- Li, T.-Y., Li, H.-C., Xiang, X.-J., Guo, Z.-X., Li, J.-Y., Zhou, F.-L., Chen, H.-L., Peng, L.-L., 2012. Transportation characteristics of $\delta^{13}\text{C}$ in the plants-soil-bedrock-cave system in Chongqing karst area. *Sci. China Earth Sci.* 42, 526–535.
- Li, T.-Y., Shen, C.-C., Huang, L.-J., Jiang, X.-Y., Yang, X.-L., Mii, H.-S., Lee, S.-Y., Lo, L., 2014. Stalagmite-inferred variability of the asian summer monsoon during the

- penultimate glacial–interglacial period. *Clim. Past* 10 (3), 1211–1219.
- Li, Y.X., Rao, Z.G., Cao, J.T., Jiang, H., Gao, Y.L., 2017. Highly negative oxygen isotopes in precipitation in southwest China and their significance in paleoclimatic studies. *Quat. Int.* 440, 64–71.
- Lisicki, L.E., Raymo, M.E., 2005. A Pliocene–Pleistocene stack of 57 globally distributed benthic $\delta^{18}\text{O}$ records. *Paleoceanography* 20, 522–533.
- Liu, D.B., Wang, Y.J., Cheng, H., Edwards, R.L., Kong, X.G., Li, T.Y., 2016. Strong coupling of centennial-scale changes of Asian monsoon and soil processes derived from stalagmite $\delta^{18}\text{O}$ and $\delta^{13}\text{C}$ records, Southern China. *Quat. Res.* 85, 333–346.
- Loutre, M.F., Paillard, D., Vimeux, F., Cortijo, E., 2004. Does mean annual insolation have the potential to change the climate? *Earth Planet Sci. Lett.* 221, 1–14.
- Maher, B.A., Thompson, R., 2012. Oxygen isotopes from Chinese caves: records not of monsoon rainfall but of circulation regime. *J. Quat. Sci.* 27, 615–624.
- McDermott, F., 2004. Palaeo-climate reconstruction from stable isotope variations in speleothems: a review. *Quat. Sci. Rev.* 23, 901–918.
- McGee, D., Donohoe, A., Marshall, J., Ferreira, D., 2014. Changes in ITCZ location and cross-equatorial heat transport at the last glacial maximum, Heinrich stadial 1, and the mid-Holocene. *Earth Planet Sci. Lett.* 390, 69–79.
- Mickler, P.J., Banner, J.L., Stern, L., Asmerom, Y., Edwards, R.L., Ito, E., 2004. Stable isotope variations in modern tropical speleothems: evaluating equilibrium vs. kinetic isotope effects. *Geochem. Cosmochim. Acta* 68, 4381–4393.
- Mickler, P.J., Stern, L.A., Banner, J.L., 2006. Large kinetic isotope effects in modern speleothems. *GSA Bull.* 118, 65–81.
- Midhun, M., Ramesh, R., 2016. Validation of $\delta^{18}\text{O}$ as a proxy for past monsoon rain by multi-GCM simulations. *Clim. Dynam.* 46, 1371–1385.
- Muschitiello, F., D'Andrea, W.J., Schmittner, A., Heaton, T.J., Balascio, N.L., deRoberts, N., Caffee, M.W., Woodruff, T.E., Welten, K.C., Skinner, L.C., Simon, M.H., Dokken, T.M., 2019. Deep-water circulation changes lead North Atlantic climate during deglaciation. *Nat. Commun.* 10, 1272.
- Nair, A., Mohan, R., Crosta, X., Manoj, M.C., Thamban, M., Marieu, V., 2019. Southern Ocean sea ice and frontal changes during the Late Quaternary and their linkages to Asian summer monsoon. *Quat. Sci. Rev.* 213, 93–104.
- NEEM Community Members, 2013. Eemian interglacial reconstructed from a Greenland folded ice core. *Nature* 493, 489–494.
- North Greenland Ice Core Project Members, 2004. High-resolution record of Northern Hemisphere climate extending into the last interglacial period. *Nature* 431, 147–151.
- Pu, J.B., Shen, L.C., Wang, A.Y., He, Q.F., Yuan, W.H., Hu, Z.Y., Chen, B.Q., He, Y., 2009. Space-time variation of hydro-geochemistry index of the Xueyu cave system in Fengdu county, Chongqing. *Carsol. Sin./Zhong Guo Yan Rong* 28, 49–54.
- Qu, T., Du, Y., Strachan, J., Meyers, G., Slingo, J., 2005. Sea surface temperature and its variability in the Indonesian region. *Oceanography* 18, 50–61.
- Ruan, J.Y., Zhang, H.Y., Cai, Z.Y., Yang, X.Q., Yin, J., 2019. Regional controls on daily to interannual variations of precipitation isotope ratios in Southeast China: implications for paleomonsoon reconstruction. *Earth Planet Sci. Lett.* 527, 115794.
- Schulz, H., von Rad, U., Erlenkeuser, H., von Rad, U., 1998. Correlation between Arabian Sea and Greenland climate oscillations of the past 110,000 years. *Nature* 393, 54–57.
- Sirocko, F., 2003. What drove past teleconnections? *Science* 301, 1336–1337.
- Spötl, C., Fairchild, I.J., Tooth, A.F., 2005. Cave air control on dripwater geochemistry, Obir Caves Austria: implications for speleothem deposition in dynamically ventilated caves. *Geochem. Cosmochim. Acta* 69, 2451–2468.
- Sun, W.W., Zhang, E.L., Shulmeister, J., Bird, M.I., Chang, J., Shen, J., 2019. Abrupt changes in Indian summer monsoon strength during the last deglaciation and early Holocene based on stable isotope evidence from Lake Chenghai, southwest China. *Quat. Sci. Rev.* 218, 1–9.
- Sun, Y.B., Wang, X.L., Liu, Q.S., Clemens, S.C., 2010. Impacts of post-depositional processes on rapid monsoon signals recorded by the last glacial loess deposits of northern China. *Earth Planet Sci. Lett.* 289, 171–179.
- Tan, M., 2014. Circulation effect: response of precipitation $\delta^{18}\text{O}$ to the ENSO cycle in monsoon regions of China. *Clim. Dynam.* 42, 1067–1077.
- Tao, S.Y., Chen, L., 1987. A review of recent research on the East Asian summer monsoon in China. *Monsoon Meteorology*. Oxford University Press, London, pp. 60–92.
- Taylor, S.R., McLennan, S.M., 1995. The geochemical evolution of the continental crust. *Rev. Geophys.* 33, 241–265.
- Walker, J.M., Bordoni, S., Schneider, T., 2015. Interannual variability in the large-scale dynamics of the south asian summer monsoon. *J. Clim.* 28, 3731–3750.
- Wang, P.X., Wang, B., Cheng, H., Fasullo, J., Guo, Z.T., Kiefer, T., Liu, Z.Y., 2017. The global monsoon across time scales: mechanisms and outstanding issues. *Earth Sci. Rev.* 174, 84–121.
- Wang, S.Y., Lu, H.Y., Han, J.T., Chu, G.Q., Liu, J.Q., Negendank, J.F., 2012. Palaeovegetation and palaeoclimate in low-latitude southern China during the last glacial maximum. *Quat. Int.* 248, 79–85.
- Wang, Y.J., Cheng, H., Edwards, R.L., An, Z.S., Wu, J.Y., Shen, C.C., Dorale, J.A., 2001. A high-resolution absolute-dated late pleistocene monsoon record from Hulu cave, China. *Science* 294, 2345–2348.
- Wang, Y.J., Cheng, H., Edwards, R.L., He, Y.Q., Kong, X.G., An, Z.S., Wu, Y.Y., Kelly, M.J., Dykoski, C.A., Li, X.D., 2005. The Holocene asian monsoon: links to solar changes and north atlantic climate. *Science* 308, 854–857.
- Weber, M.E., Clark, P.U., Kuhn, G., Timmermann, A., Sprenk, D., Gladstone, R., Zhang, X., Lohmann, G., Menzel, L., Chikamoto, M.O., Friedrich, T., Ohlwein, C., 2014. Millennial-scale variability in Antarctic ice-sheet discharge during the last deglaciation. *Nature* 510, 134–138.
- Xu, S.Q., Yang, P.H., Yin, J.J., Mao, H.H., Wang, P., Zhou, X.P., 2013. Research on the sensitivity of geochemical of underground River in Chongqing Xueyu cave. *Environ. Sci.* 34, 77–83.
- Xue, J.B., Zhong, W., Xie, L.C., Unkel, I., 2015. Vegetation responses to the last glacial and early Holocene environmental changes in the northern Leizhou Peninsula, South China. *Quat. Res.* 84, 223–231.
- Yang, H., Johnson, K.R., Griffiths, M.L., Yoshimura, K., 2016. Interannual controls on oxygen isotope variability in Asian monsoon precipitation and implications for paleoclimate reconstructions. *J. Geophys. Res.: Atmos.* 121, 8410–8428.
- Yonge, C.J., Ford, D.C., Gray, J., Schwarcz, H.P., 1985. Stable isotope studies of cave seepage water. *Chem. Geol.* 58, 97–105.
- Yuan, D.X., Cheng, H., Edwards, R.L., Dykoski, C.A., Kelly, M.J., Zhang, M.L., Qing, J.M., Lin, Y.S., Wang, Y.J., Dorale, J.A., An, Z.S., Cai, Y.J., 2004. Timing, duration, and transitions of the last interglacial asian monsoon. *Science* 304, 575–578.
- Zhang, H.B., Griffiths, M.L., Huang, J.H., Cai, Y.J., Wang, C.F., Zhang, F., Cheng, H., Ning, Y.F., Hu, C.Y., Xie, S.C., 2016. Antarctic link with East Asian summer monsoon variability during the Heinrich Stadial-Bolling interstadial transition. *Earth Planet Sci. Lett.* 453, 243–251.
- Zhang, H.W., Ait Brahim, Y., Li, H.Y., Zhao, J.Y., Kathayat, G., Tian, Y., Baker, J., Wang, J., Zhang, F., Ning, Y.F., Edwards, R.L., Cheng, H., 2019. The asian summer monsoon: teleconnections and forcing mechanisms—a review from Chinese speleothem $\delta^{18}\text{O}$ records. *Quaternary* 2, 26.
- Zhang, J., Li, T.-Y., 2019. Seasonal and interannual variations of hydrochemical characteristics and stable isotopic compositions of drip waters in Furong Cave, Southwest China based on 12 years' monitoring. *J. Hydrol.* 572, 40–50.
- Zhang, J.W., Liu, S.S., Liu, D.B., Kong, X.G., Fang, Y.F., 2019. Correlation between oxygen and carbon isotopes of speleothems from Tian'e Cave, central China: insights into the phase relationship between Asian summer and winter monsoons. *J. Asian Earth Sci.* 180, 103884.
- Zhang, T.-T., Li, T.-Y., Cheng, H., Edwards, R.L., Shen, C.-C., Spötl, C., Li, H.-C., Han, L.-Y., Li, J.-Y., Huang, C.-X., 2017. Stalagmite-inferred centennial variability of the Asian summer monsoon in Southwest China between 58 and 79ka BP. *Quat. Sci. Rev.* 160, 1–12.
- Zhao, K., Wang, Y.J., Edwards, R.L., Cheng, H., Liu, D., 2010. High-resolution stalagmite $\delta^{18}\text{O}$ records of Asian monsoon changes in central and southern China spanning the MIS 3/2 transition. *Earth Planet Sci. Lett.* 298, 191–198.
- Zhu, 2012. Variations of the summer Somali and Australia cross-equatorial flows and the implications for the asian summer monsoon. *Adv. Atmos. Sci.* 29, 509–518.
- Zhu, X.W., Zhang, Y.H., Han, D.S., Wen, R.P., Chen, B.Q., 2004. Cave characteristics and speleothems in XueYu cave group, Fengdu, Chongqing city. *Carsol. Sin./Zhong Guo Yan Rong* 23, 85–90.